Improving Magnetic Map-Based Navigation using Vehicle Motion Information

by

Ryan Scott McWilliams

A thesis submitted to the Graduate Faculty of
Auburn University
in partial fulfillment of the
requirements for the Degree of
Master of Science

Auburn, Alabama
May 7, 2022

Keywords: Magnetic, GNSS-denied, Map-Matching

Approved by

David Bevly, Chair, Bill and Lana McNair Endowed professor
Scott Martin, Assistant Professor of Mechanical Engineering
Howard Chen, Assistant Research Professor of Mechanical Engineering

Abstract

This thesis utilizes the earth's main magnetic field as the signal for a map definition, implements a particle filter to synthesize a solution from likelihood information, and introduces vehicle motion information by means of velocity and heading measurements to augment the traditional filter structure. Three different process models are investigated: Gauss-Markov, a known capable technique in which particles evolve stochastically; wheel speed linear motion with magnetometer heading updates, in which the particles attempt to imitate the movement of the vehicle using a heading derived from magnetic north (with declination correction); and wheel speed linear motion with gyroscope heading updates, in which angular velocity measurements are integrated to update the heading at every time step instead. Measurement updates were performed with respect to the map and the local magnetic signal. Two nominal routes were evaluated using the Gauss-Markov approach as a baseline and the root-mean-square error in the position estimate compared to that of the motion-informed models. Results show that vehicle odometry can decrease the error in the position solution by between 22% and 77% on average and decrease the typical maximum error along a route by about 54%. This focus was expanded to explore non-nominal driving conditions including a map driven in reverse, a map featuring a short detour, and a map featuring a large detour. In these cases, every filter implementation struggled to track the vehicle once it exited the map, but recovery was possible in some instances when the vehicle returned to a known or strongly identifiable region.

Acknowledgments

I would like to dedicate this thesis to my parents Mark and Kathy. This thesis would not have been possible without their enduring love and support. I would also like to thank my brother Daniel for his guidance and wisdom and for always helping me to become a better engineer and programmer. Additional gratitude is due to Matthew Thompson, my International Baccalaureate teacher of English and Theory of Knowledge, for instilling in me a curious mind and desire for understanding.

I also would like to recognize the many intelligent and remarkable coworkers that I have had the opportunity to meet, work with, and learn from at the GPS and Vehicle Dynamics Laboratory. Firstly is Dr. Howard Chen, who has provided professional advice and personal friendship throughout my time in graduate school. His mentorship greatly shaped my work and my development as an engineer and researcher. Next are the many members of the GAVLAB's first-floor work space, lovingly termed 'the Dungeon,' for their companionship, insight, and diligence: Stephanie Meyer, David Bell, Christian Campos-Vega, Trenton Hilyer, Tyler Flegel, and Gregory Mifflin. Each of them helped me to expand my horizons, support my ambitions with hard work, and to always remember the joy of asking and answering questions however serious or silly. Similarly, thank you to the members of the main lab and residents of the GAVLAB's new home at the MRI building for their time and attention discussing many different research topics and for occasional, pleasant distractions.

Also deserving of recognition are Brendan Schretter, for his help understanding hardware interfaces and sensor data critical to this thesis and other work across the GAVLAB, and Kyle Thompson for his help operating the Lincoln MKZ used for data collection.

Special recognition is deserved to Archit Thopay, who introduced me to the people and work of the GAVLAB before I had even completed undergrad and who convinced me to pursue this rewarding course, and to our mutual roommate Jonathan Lawley for sharing his encouragement and determination. Thanks as well to my longtime friends Nolen Murphy and Melissa

Shuford for believing in me and my work, even when I struggled to do so. And of course to my beloved feline friends Ginger, Little Bit, and Mitsy, who provided an abundance of humor and carefree companionship.

Finally, I would like to thank my advisors and committee members, Dr. David Bevly, Dr. Scott Martin, and again Dr. Howard Chen for reviewing this document and advising me throughout my time in graduate school. They have allowed me to grow into a better engineer, researcher, and person, and I will forever be grateful.

"Every great advance in science has issued from a new audacity of imagination." – John Dewey

Table of Contents

List of Figures

Chapter 1

Introduction

1.1 Motivation

The topic of navigation has interested explorers and scientists for centuries, dating back to at least 3000 BC [2]. Merriam-Webster gives the definition of *navigation* as "the science of getting ships, aircraft, or spacecraft from place to place" [3]. Within this definition are the disciplines of *positioning* (sometimes also called *localization*), which consists of placing a moving object with respect to a known reference frame; and *guidance*, which involves the determination of a desired trajectory for that moving object to follow. This work will focus on the former discipline.

The need for more precise, accurate, and reliable means of navigation has increased over time as other technologies have allowed humans to traverse space farther and faster and brought about a tightly-connected world. Furthermore, this need has manifested at multiple scopes: pedestrians, ground vehicles, aircraft, and spacecraft each require comprehensive solutions, often in real time. Fortunately, modern navigators are capable of leveraging powerful computers and microelectronics to provide high-quality solutions. Chief among the most popular navigation technologies applicable at each scope is the global navigation satellite system (GNSS), developed in the 20th century and since implemented by multiple state governments around the world. GNSS-based navigation solutions can provide any sufficiently equipped user with a quick, stable, externally-referenced position for themselves or their platform. Moreover, the necessary communications and computation hardware has been successfully miniaturized and is now nearly ubiquitously present in consumer smart phones.

Despite widespread use, GNSS is fundamentally vulnerable to disruption both from deliberate actors via jamming or spoofing [4], and from environmental factors such as urban canyons and dense foliage [5]. In some instances performance is only degraded but sufficient disturbances can block a solution from being derived at all. These threats will only grow more prominent in the coming years as populations grow and threat-capable equipment becomes more accessible. To preempt these threats, parties interested in navigation continue to investigate ways of mitigating these susceptibilities and to develop alternative methods that do not share these failure modes, collectively termed "GNSS-denied navigation."

Alternatives to GNSS make up a broad and active field of research and several potential solutions have been proposed. The most classical approach is dead reckoning using inertial sensors, in which the motion of the vehicle or object is measured and integrated to estimate a trajectory which is applied to the previous position estimate [6]. However, these trajectories are subject to a time-dependent error which can grow exceedingly large without correction. Inertial navigation is commonly used in conjunction with GNSS to improve localization estimates, with the error only becoming a function of time when GNSS outages occur. However, in the case of consumer-grade inertial measurement units, a GNSS outage of less than a minute is enough to noticeably affect the localization solution [7].

Another method of navigation capable of providing solutions independently or in cooperation with GNSS is optical navigation, which employs cameras or light detection and ranging (LIDAR) sensors to interpret the navigation environment [8]. Research has show that optical navigation techniques can provide precise and accurate localization estimates, but that results are dependent on environmental factors such as illumination, typically require greater computational resources than inertial or GNSS methods, and may require expensive equipment (either sensors or mounting schemes) that is not readily available for practical applications [9].

Magnetic fields as a sensing modality has shown practical value already thanks to previous research on the topic. Magnetic fields are naturally occurring and are easy to measure with a baseline signal that is fairly constant [10]. Although magnetometers have long been used to estimate heading– most primitively as the humble navigational compass dating to at least the 11th century [11]– newer research has shown that local magnetic fields can be mapped to

2

known locations and subsequently used as a source of information for localization [12]. In contrast to inertial-based navigation, this approach has the benefit of error characteristics that are time-invariant. Unlike optical-based navigation, magnetic fields are a much less data-intensive signal and are not affected by external varying factors such as illumination [13]. As an additional advantage, magnetometers are relatively inexpensive to manufacture and incorporate. Often, magnetometers are already included in many inertial navigation systems for heading estimation. Furthermore, magnetic localization has been successfully tested indoors and outdoors for multiple vehicle types and has achieved errors on the order of tens of meter for ground vehicles [14] and hundreds of meters for aerial vehicles [15].

Although promising, map-based navigation does present unique challenges for both pre-processing of map data and solution generation. Typically, map-based navigation requires extensive pre-processing of data to interpret and format information appropriately. For some applications, map data may be publically available. For example, barometric maps correspond closley with easily-accessible Digital Elevation Maps and numerous private and public sources exist for such information [16]. The World Magnetic Model is capable of providing information useful for navigation in limited contexts, such as for aerial vehicles. For ground vehicles, temporary and permanent variances due to human activity require bespoke magnetic maps to be constructed in advance of navigation attempts. This limits the applicable scope to known or expected routes about an area. Moreover, the navigator is conventionally expected to follow the mapped route as closely as possible to achieve sufficient performance; however, this is not reflective of real-world use cases in which mistakes or deliberate divergences from mapped routes are common.

Even in relatively constrained and discernible conditions it is extrememly likely that a navigator will encounter distinct but numerically similar magnetic measurements, requiring any navigation algorithm to resolve ambiguities robustly. These ambiguities may be overwhelmingly present in routes with few dynamics in the magnetic measurements; for example, mapped paths which follow an iso-magnetic line and do not encounter distinguishable magnetic features. In this case, the signal is said to contain insufficient *spatial-frequency*. Incorporating additional sensor measurements, such as the linear and angular velocities of the vehicle, may

provide information useful to limiting or reducing solution errors [17]. Because map-matching does not typically constrain solutions to a motion model, velocity or acceleration information may function to effectively bound the number of viable solutions and increase filter performance [18].

1.2 Contributions

Localization of ground vehicles by magnetic maps is a technology in need of additional development to gauge performance profiles and to establish the environmental contexts and supplemental technologies necessary to generate practical outcomes. To expand upon this subject and facilitate more accurate and more reliable navigation systems, this thesis:

1. Examine quantitatively the signals of magnetometer and inertial sensors and associated maps to establish potential for improvement by fusion.

2. Defines and augments a particle filter to utilize magnetic, inertial, and wheel-encoded information in the generation of a navigation solution.

3. Evaluates performance in off-route conditions and recoverability in the event of failure or divergence.

1.3 Thesis Outline

This thesis has seven remaining chapters:

Chapter 2 provides the technical background for the work, including an examination of the magnetic signal foundation, the coordinate frames used, and the mathematical foundations for dead reckoning and particle filtering.

Chapter 3 reviews the data collection system consisting of the vehicle platform and sensors, the locations and routes selected for data collections, and steps taken to interpret magnetic signals into a navigable map.

Chapter 4 reviews the assumptions made in the dead reckoning implementation of this research and evaluates mechanization performance using the sensors discussed in the previous chapter.

Chapter 5 discusses techniques to produce localization solutions using the magnetic map-matching approach.

Chapter 6 presents the particle filter to augment solutions using various models of particle propagation to emulate vehicle motion.

Chapter 7 extends the scope of the research to include contingency navigation conditions, namely when a map is inaccurate or piloting is imprecise.

Chapter 8 summarizes the findings of this thesis, draws conclusions, and describes future work.

Chapter 2

Technical Background

2.1 Magnetic Field Definition

Geomagnetism– the magnetic field generated by the Earth liquid outer core– is of particular interest to navigators and researchers as it provides a reliable and readily available signal that can be used to attain heading and position information. This phenomenon occurs naturally and is detectable at any conventionally traversable altitude from the planet's surface, but the amplitude and direction of the magnetic field is significantly less than everyday magnets and requires a magnetometer to gauge [10].

A measurement of a magnetic field is comprised of a vector representing the field strength in three orthogonal directions. Specifically, the quantity of interest is the "magnetic flux density," commonly represented by the unit 'Gauss.' Some literature sources instead report this quantity in the SI-approved unit of Tesla, which is defined as 10^4 Gauss. The earth's main magnetic field typically fluctuates in absolute intensity between 0.3 and 0.6 Gauss depending on the sensor's location with respect to the poles and the equator [19].

The earth's main magnetic field is described by several components: declination, inclination, horizontal intensity, vertical intensity, total intensity, and the north and east subcomponents of the horizontal intensity. For a given location about the earth, the world magnetic model determines these components by a high-order spherical harmonic expansion of the magnetic scalar potential function. Due to the evolving nature of the earth's magnetic field, these values are not constant and the model is updated regularly to reflect changes and predict future

variations within a limited time window; however, it remains a reliable source for navigation within the most recent window of viability.

An object or vehicle's heading as an angle from magnetic north can be derived by calculating the arctangent using magnetic measurements in vehicle's lateral and forward directions, respectively. Additionally, even given perfect measurements, the heading solution will typically differ from true north because the *declination*, or the relative angle between true and magnetic north, will reflect their different positions on the earth. This can be corrected for using the declination value provided that the geodetic position is known by applying the World Magnetic Model. Figure 2.1 displays lines of constant declination in degrees over a world map as supplied by the World Magnetic Model for 2020-2025, a publically available technical report issued by the US National Geospatial Intelligence Agency and the UK Defence Geographic Center which charts the characteristics of the Earth's magnetic field [1].

At the ground-vehicle scope, variations and disturbances are almost always evident in the main magnetic signal. These disturbances can be beneficial or detrimental to navigation depending on their temporal nature. In some cases, a permanent structure or item may provide a unique disturbing effect, resulting in an easily-matchable measurement when the structure or item is approached again. Examples could include a metal pipe near a roadway. Temporary sources of disturbances, such as nearby car traffic or on-board electronics, instead negatively interfere with the signal because they are not consistently repeatable [14]. Longer-term temporary variances, such as seasonal or annual changes, may impact the dependability of magnetic records in ways not well understood for map-matching purposes.
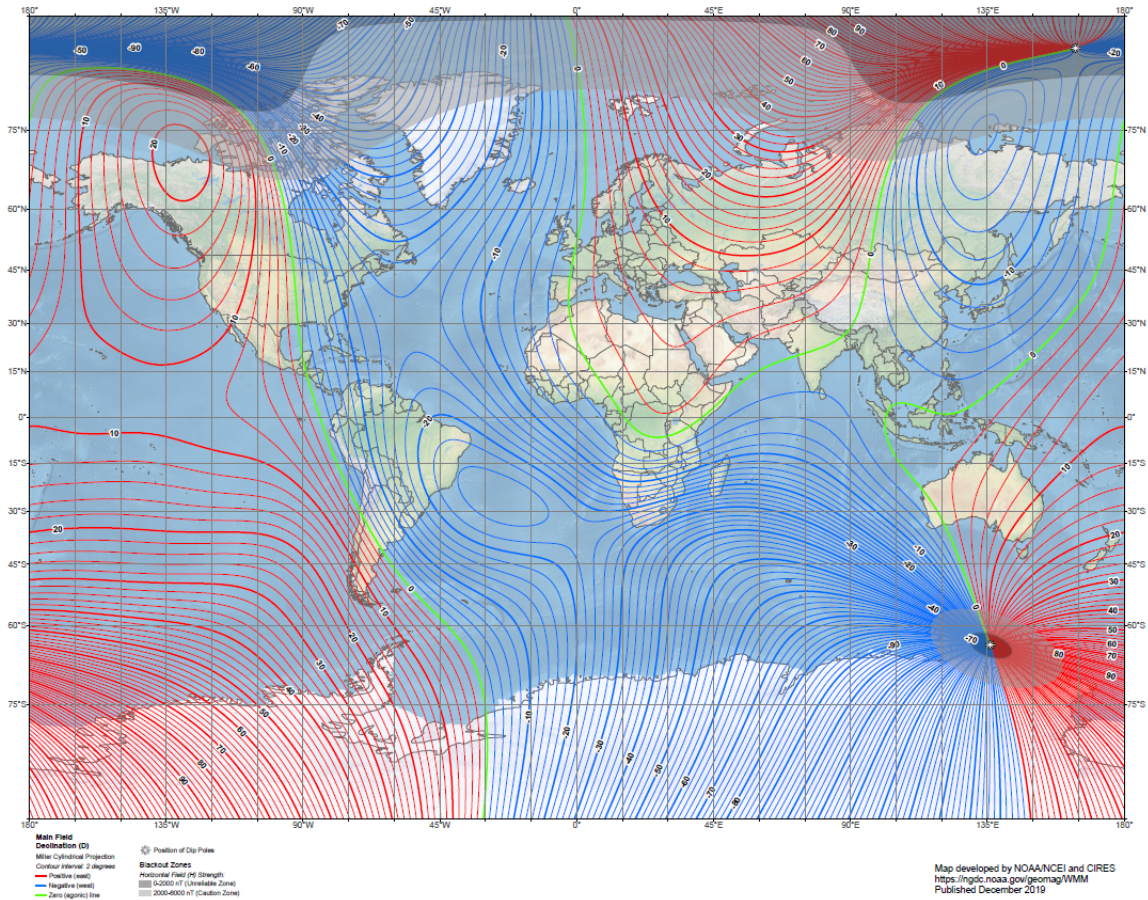
Figure 2.1: Lines of equivalent declination plotted over a map of the globe [1]
.

2.2 Coordinate Frames and Transformations

Coordinate frames provide the physical context for quantitative measurements and knowledge of their implementation is critical to navigation. Practical use cases require the synthesis of multiple frames of reference to produce a useful solution.

Most commonly, right-handed orthogonal three-dimensional coordinate systems are employed to describe the vectors associated with an object or vehicle of interest. When two reference frames are employed, an object or vehicle of interest *A* is described according to its relationship to a known body or point *B*. It is said then that "*A* has a position and orientation with respect to *B*." In the event that a third reference frame is also employed, *C*, then "*A* has a position and orientation with respect to *B* resolved in *C*," or just "in *C*." When discussing a

value or vector in the context of reference frames, the former two frames are represented as subscripts begining with the known body or point and the latter frame (when relevant) is represented in superscript; for example, a force on object A with respect to frame B resolved in frame C is written F_{BA}^{C}. Next is a discussion of the coordinate frames applied in this research and how transformations between coordinate frames were obtained [6].

2.2.1 Inertial Frame

The inertial frame is defined to be a non-accelerating frame of reference and is typically the coordinate frame in which accelerations and angular velocities are specified. The earth-centered inertial frame (ECI), denoted by i, serves as the inertial coordinate system for this research. The origin of the ECI frame is located at the planet's center of mass but does not rotate with the earth. As a result, a 'static' gyroscope that is not moving with respect to the surface will still record and angular velocity measurements corresponding to the earth's rotation; however, but for the highest-quality instruments these measurements are smaller or similar in scale to the effects of noise and bias. Gravitational acceleration is also evident in accelerometer measurements but must be identified and removed where necessary due to its magnitude. The ECI frame is an acceptable assumption for ground vehicle navigation because ground vehicles rarely travel far enough or fast enough for the influence of the earth's rotation to be greater in significance than instrumentation errors.

2.2.2 Sensor Body Frames

Both the HMR2300 and the VN-300 sensors were mounted rigidly in the trunk area of the vehicle by tightly fitting the flanges of the sensors' casings between either bolts or screws which fastened to a metal lattice structure, itself tightly fixed internally to the body of the vehicle. Each sensor has its own right-handed coordinate frame with respect to which measurements are recorded. Senors were mounted with the intention of allowing for easy transformation of measurements from the sensors' respective frames to the vehicle body frame.

The measured specific force specified by the nomenclature $\tilde{f}^b_{ib,x}$ is read as "the specific force f of the body frame with respect to the inertial frame resolved in the body frame". The angular $\tilde{\omega}^b_{ib,x}$ is read similarly. The VN-300 IMU recorded data in 3 dimensions such that one IMU measurement for any given moment in time consists of $\{\tilde{f}^b_{ib,x}, \tilde{f}^b_{ib,y}, \tilde{f}^b_{ib,z}\}$ and $\{\tilde{\omega}^b_{ib,x}, \tilde{\omega}^b_{ib,y}, \tilde{\omega}^b_{ib,z}\}$.

2.2.3 Vehicle Body Frame

The goal of this research is not to estimate the motion and orientation of the sensors themselves, but of the vehicle to which they are afixed. It is therefore necessary to define the vehicle body frame and to rotate sensor measurements into this frame. The vehicle frame was defined with the x-axis extruding out the front of the vehicle ('forward' or 'longitudinal'), the y-axis out the driver-side door ('left' or 'lateral'), and the z-axis upward ('up') through the roof of the vehicle. Rotations about these axes are referred to as roll (ϕ), pitch (θ), and yaw (ψ), respectively. The sign of rotation angles are defined according to the right-hand rule. This frame is denoted by b.
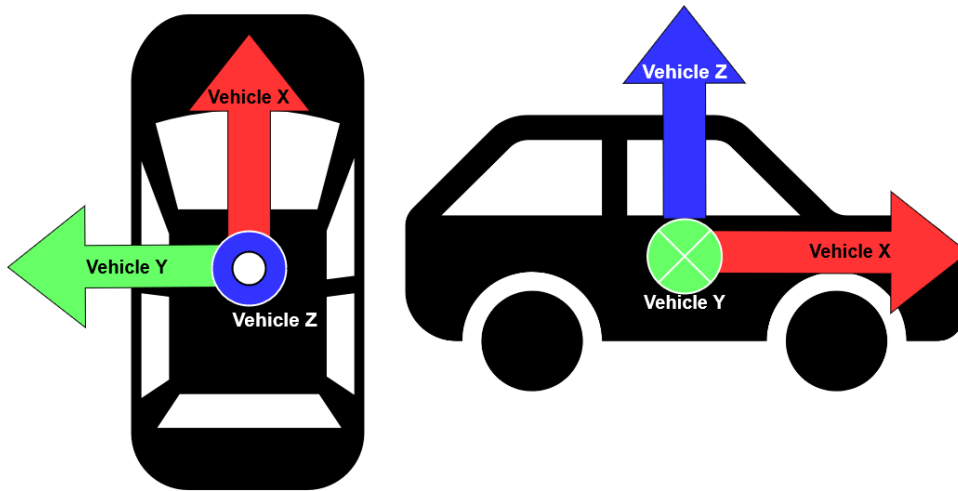
Figure 2.2: Vehicle Frame: From the driver's point of view, X represents 'Forward,' Y represents 'Left,' and Z represents 'Up.'

2.2.4 Geodetic Frame

The GPS data used in this research was measured in a geodetic coordinate system before it was converted to the local navigation frame. The geodetic frame is a curvilinear orthogonal coordinate system in which a position is described by a latitude and longitude, typically measured in degrees from a standard datum, as well as a height in meters. This research assumes

a geodetic system to represent the Earth with a longitudinal datum at the prime meridian, a latitudinal datum at the equator, height measured from the surface of the earth as given by the World Geodetic Model published in 1983 ('WGS 84') [6]. The geodetic frame is also the basis for the World Magnetic Model and is used to determine the declination angle between magnetic north and true north in heading estimation.

2.2.5 Navigation Frame

The local navigation frame is the reference frame in which a navigation solution is resolved and is typically defined with respect to a point on the Earth's surface, using either a North-East-Down (NED) or East-North-Up (ENU) axes convention. In the latter convention, east is treated as the x-axis and north as the y-axis. The z-axis, which would correspond to the direction 'Up,' was not included in the navigation solution; however, the nature of ground vehicles allows users to assume the vehicle is at the same height as the road which commonly corresponds with the surface of the earth or nearby infrastructure.
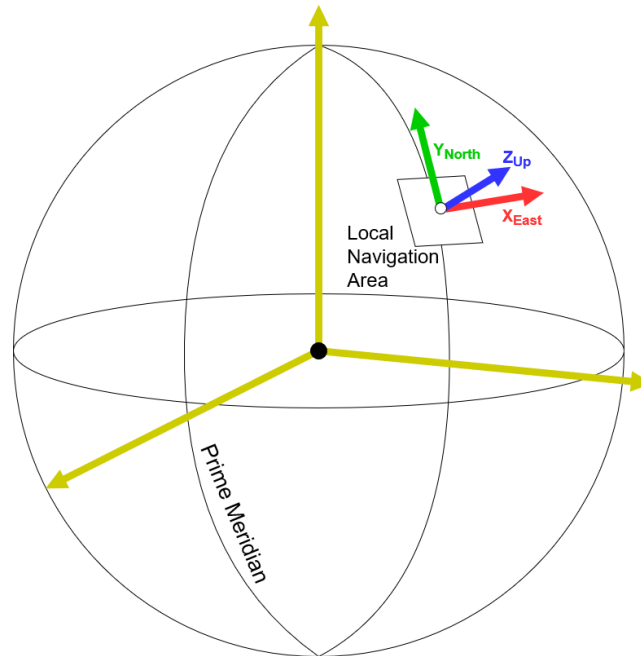
Figure 2.3: ECI and Local Navigation Frames.

2.2.6 Transformations

Throughout this research, it was sometimes necessary to place data or measurements in a reference frame different from the one in which they were initially recorded. In these instances, a coordinate transformation matrix was utilized. Specifically, the mounting of the IMU and magnetometer each resulted in a permanent, fixed attitude with respect to the vehicle frame.

The *attitude* or *orientation* of an object or frame with respect to another is defined as the relative angular difference between them, most commonly represented by three *Euler angles*: Yaw, 'ψ,' about the initial z axis; Pitch, 'θ,' about the initial y axis; and Roll, 'ϕ,' about the initial x axis. To apply these rotations to a vector measured in one frame, they are implemented as matrices which are pre-multiplied by the vector to be rotated [20]. For the given euler angles and axes of rotation, the rotation matrices are:

$$C_z = \begin{bmatrix} cos(\psi) & sin(\psi) & 0 \\ -sin(\psi) & cos(\psi) & 0 \\ 0 & 0 & 1 \end{bmatrix} \tag{2.1}$$

$$C_y = \begin{bmatrix} cos(\theta) & 0 & -sin(\theta) \\ 0 & 1 & 0 \\ sin(\theta) & 0 & cos(\theta) \end{bmatrix} \tag{2.2}$$

$$C_x = \begin{bmatrix} 1 & 0 & 0 \\ 0 & cos(\phi) & sin(\phi) \\ 0 & -sin(\phi) & cos(\phi) \end{bmatrix} \tag{2.3}$$

In the event that rotation occurs about multiple axes, the individual rotation matrices can be multiplied to provide a succint, overall transformation matrix:

$$C_{zyx} = \begin{bmatrix} c(\psi)c(\theta) & c(\theta)c(\psi) & -s(\theta) \\ c(\psi)s(\phi)s(\theta) - c(\phi)s(\psi) & c(\phi)c(\psi) + s(\phi)s(\psi)s(\theta) & c(\theta)s(\phi) \\ s(\phi)s(\psi) + c(\phi)c(\psi)s(\theta) & c(\phi)s(\psi)s(\theta) - c(\psi)s(\phi) & c(\theta)c(\phi) \end{bmatrix} \tag{2.4}$$

Because vehicle-based sensors will measure with respect to the vehicle frame, this transformation is most often evaluated and applied with respect to the body frame to place data in the navigation frame.

Matrix mutliplication is not commutative, so the order in which these rotations are carried out is critical. Here, we have utilized a standard *ZYX* order and will do so throughout the paper, though other standards exist. One drawback of the *ZYX* implementation is the phenomenon of *gimbal lock* in which a singularity occurs when the value of the pitch angle is equal to $\pm 90°$, causing a lack fo distinction in measurements between roll and yaw. Thankfully, this is rarely encountered for ground vehicle applications.

2.3 Dead Reckoning

Dead reckoning refers to a method of position estimation by applying the integral of either a change in position or a change in velocity and to a previously known position fix [6]. Modern sensors include tachometers or wheel-speed motor encoders and inertial measurement units. If the latter is utilized and the linear accelerations and angular velocities it records are integrated to resolve a change in position and orientation, the method is called *inertial navigation*. Equations 2.5 and 2.6 show the linear update equations, where $\boldsymbol{p}$ is the position vector, $\boldsymbol{v}$ is the velocity vector, and $\boldsymbol{\omega}$ is the angular velocity vector:

$$\boldsymbol{p}^+ = \boldsymbol{p}^- + \dot{\boldsymbol{p}}\Delta t \tag{2.5}$$

$$\dot{\boldsymbol{p}} = \boldsymbol{v} \tag{2.6}$$

$$\boldsymbol{\omega} = \begin{bmatrix} \dot{\phi} & \dot{\theta} & \dot{\psi} \end{bmatrix} \tag{2.7}$$

Placing measurements into the navigation frame using the transformation matrix C_V^N and integrating to determine a position solution is known as *mechanizing* the data. This requires the transformation matrix to be updated by the angular velocity vector:

$$\dot{C}_V^N = C_V^N [(\boldsymbol{\omega})^\wedge] \tag{2.8}$$

$$(C_V^N)^+ = (C_V^N)^- + \dot{C}_V^N \Delta t \tag{2.9}$$

where $[(\boldsymbol{\omega})^\wedge]$ is the skew-symmetric matrix realization of the angular velocities.

In reality, this method will compound sensor errors over time, resulting in a divergent error in the position solution:

$$\delta\dot{\boldsymbol{p}} = \delta\boldsymbol{p} + \delta\boldsymbol{v} \tag{2.10}$$

For a real signal z, any sensed measurement $\tilde{z}$ is modeled by a stochastic noise term η and a bias term b.

$$\tilde{z} = z + \eta_z + b_z \tag{2.11}$$

The noise term is assumed to be zero-mean, normal, and Gaussian. The bias term may be constant or may be time-varying, colloquailly a 'walking' bias. These error dynamics affect both linear and angular sensors at a magnitude determined by the quality of the hardware and the calibration techniques applied to the sensor.

One of the primary goals of sensor fusion is the opportunity to utilize measurements of external phenomenon to bound or reduce these errors. Numerous means of sensor fusion exist, including the Kalman filter and its extended and unscented variants. One of the most powerful means to synthesize disparate data is the particle filter, which is discussed in general the next section and in detail for this thesis in chapter 6.

2.4   Particle Filter

The particle filter, first described in 1993 [21], is a monte carlo algorithm that allows for the estimation of systems featuring nonlinear and non-Gaussian distributions by representing a sample of the distribution space as particles, x, in the set $\boldsymbol{X}$. The number of particles, n, is an arbitrary parameter of the filter:

$$\boldsymbol{X} = x^{(i)} : i = 1...n \tag{2.12}$$

Each particle, $x^{(i)}$ is evaluated by some likelihood function utilizing a measurement z to assign it a weight value, w, which is commonly normalized to lie between 0 and 1:

$$w^{(i)} = p(x^{(i)} \mid z) \tag{2.13}$$

such that,

$$\sum_{i=1}^{n} w^{(i)} = 1 \tag{2.14}$$

At each time step, particles propagate according to some process function f given the previous particle state and some model term μ. This provides an estimate of the hidden true states, $\bar{x}$, at each sequential time step k:

$$x_k^{(i)} = f(x_{k-1}^{(i)}, \mu) \tag{2.15}$$

$$\bar{x}_k = g(\boldsymbol{X}_k, W_k) \tag{2.16}$$

With enough iterations, all particle filters inevitably encounter the problem of *degeneracy* [22]. Particle degeneration occurs when a very small number of particles are responsible for the vast majority of weight values across the particle set; e.g. when only one or a handful of particles have non-zero associated weights. This can be rectified by a resampling function R, invoked either regularly or intermittently according to some condition, in which the particle set is replaced with a sampling of the particle distribution at the most recent time step:

$$\boldsymbol{X}^+ = R(\boldsymbol{X}^-) \tag{2.17}$$

Chapter 3

Data Collection & Preparation

3.1 Data Acquistion Equipment

3.1.1 Vehicle Platform

The platform employed for data collection was a Lincoln MKZ outfitted with a Honeywell HMR2300 magnetometer and a Vectornav VN-300 INS/GNSS unit, with a patch antenna magnetically secured to the roof of the vehicle approximately above the rear driver-side seat. Figure 3.1 shows the vehicle and highlights the location of the patch antenna on its exterior. This vehi-
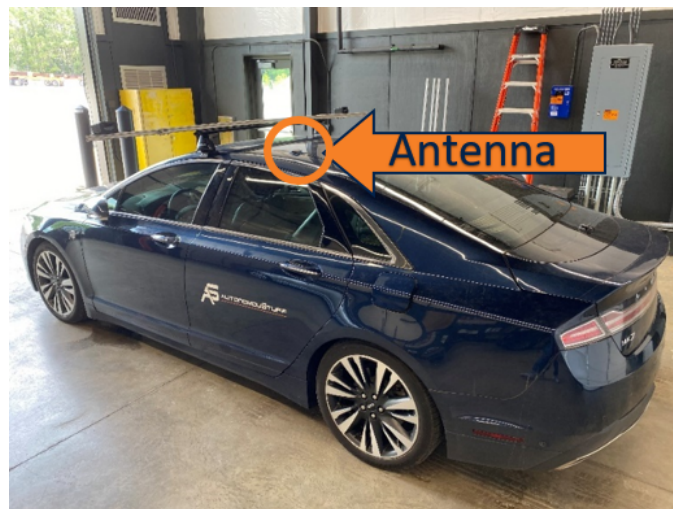
Figure 3.1: Data Collection Platform (Lincoln MKZ) with Antenna location highlighted.

cle was chosen for its availability and utility for mounting and communicating with the sensors needed to collect data, thanks to an external computer running linux located in the trunk of the vehicle and a linked internal computer interfacing with additional sensors.

3.1.2 Sensor Selection

Magnetometer

The magnetometer selected for this research was the Honeywell HMR2300 magnetometer. The HMR2300 is capable of sensing within a range of ± 2 Gauss with a resolution of 70 μGauss and high accuracy at a recording rate of 50 Hertz [23]. This range is larger than is typically necessary for sensing the Earth's natural magnetic field; however, it may prove beneficial when encountering artificial sources or disturbances. The exceptional sensitivity provided by the sensor's resolution and accuracy benefit the mapping and navigation use cases. Additionally, this matches the model of magnetometer used in similar previous studies [14].

Figure 3.2: The Honeywell HMR2300 magnetometer.

Accelerometer, Gyroscope, and GPS

Both IMU and GPS measurements were provided by the Vectornav VN-300 GNSS/INS unit. The VN-300 supplied acceleration measurements with a noise density of $5.5 \times 10^{-3} \frac{m}{s^2}$ and angular velocity measurements with a noise density of $2.4 \times 10^{-4} \frac{rad}{s}$, both at a rate of 16 Hertz, and geodetic measurements within 1 meter RMS also at a rate of 16 Hertz [24]. Neither acceleration nor gyroscope nor GPS measurements were modified or compensated by the VN-300's

optional internal Kalman filter. Although the VN-300 also features an internal magnetometer, this data was not utilized in the filter.
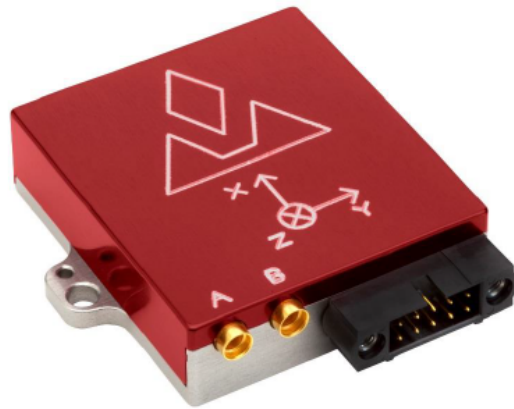
Figure 3.3: The VectorNav VN-300 GNSS/INS Unit.

Wheel Speed Encoder

Lastly, the rate of rotation of each of the wheels on the Lincoln MKZ was measured by a TMCS1100 hall-effect sensor, relayed by the internal computer and recorded in radians per second at approximately 100 Hertz with an expected accurace within $\pm 0.51\%$ of the true value [25]. This data was synthesized into a single vehicle velocity estimate by averaging the rotation speed of all four wheels and multiplying the result by the average circumference of the wheel and tire to produce an approximation in meters per second. The approximate vehicle speed as a function of the average wheel speed in radians per secont, ω, is: $\tilde{v}_{vehicle} = \omega * r$, resolved in meters per second. Emprical data collected for this research measured an average tire radius of $r = 0.3288$ meters for the data collection vehicle.

3.2   Routes

Two candidate locations were selected to be the basis for map generation. The first location, south of Auburn Unviersity's campus, was selected for its ease of access, relatively light traffic, and because the two straight-away sections to the North and East would make for good comparison with the consistent curve for most of the south and west of the area. The second location, east of Auburn University's campus, featured more active traffic and potentially more

disruptions to the magnetic signal; however, it also had available to it two roads useful for testing off-route navigation conditions: A brief stretch of road which diverges and then reconnects, useful for the 'Detour' use case; and another road that bypasses the eastern straight-away and connects to the road running northeast, which was useful for the 'Shortcut' use case. Both of these digressions from the main routes were sourced for navigation data sets but were not used to construct maps. Instead, the two previous routes were retained as the sources of the maps, creating a deliberate incongruity between mapping and navigation data sets. This was done to investigate how well or poorly the filter may fair when the vehicle does not drive along the mapped route. Each location and the route used for map generation is displayed in Figures 3.4 and 3.5. The clockwise circular arrows indicate the direction of travel.

Figure 3.4: Route 'VCOM,' beginning near the southeast corner.
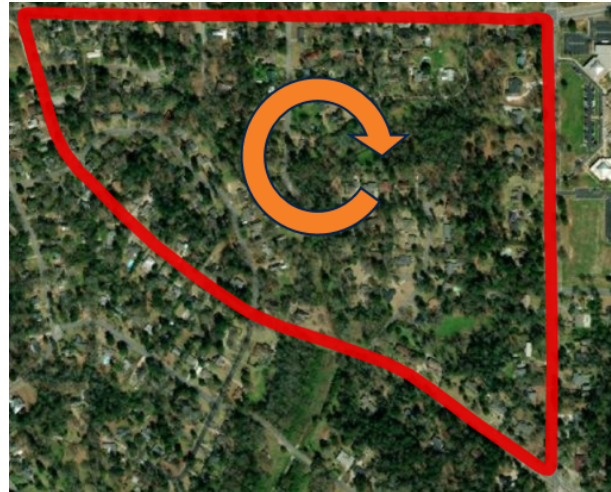
Figure 3.5: Route 'Eastside,' beginning near the northwest corner.

3.3   Data Pre-Processing

Magnetic map-based navigation requires the methodical synthesis of data to produce reliable solutions. A pre-processing step is undertaken to generate navigable maps, regulate the magnetic signal, and to mitigate errors.

3.3.1 Map Source Signals

The implementation of maps for navigation of a person or vehicle is not a novel technique. Traditionally, a map is used by navigators by matching their position relative to a known feature, landmark, label, or description provided by the map data set. However, better measurement and data handling technology has allowed for maps to be developed using more abstract indicators. These new potential sources for maps include barometry, ambient light, road noise, and– perhaps most promisingly– magnetic fields [18].

Map-based navigation requires two data sets to produce a solution:

1. A 'Map' data set, in which some measurement or phenomenon is associated with a particular position in space.

2. A 'Navigation' data set, being the measurements or observations that are in some way compared to the map data set to resolve a position solution.

For *magnetic* map-based navigation, both data sets utilize magnetic field measurements as the underlying signal for association and comparison. The position association step in the generation of the map data set is dependent on some external localization method. In this research, GNSS was utilized to provide the position associations for the map data set. This utilization does not violate the GNSS-denied interests of the research because GNSS signals are not necessary once the map is generated. Still, this does leave the technology as less GNSS-dependent, rather than wholly independent. More expensive gps-denied technologies such as optical navigation may be applied instead to complete the GNSS independence of map-based navigation.

Figure 3.6 shows the concept of operations for map-based navigation, including the two necessary parts and the simultaneous and sequential steps to generate a position solution.
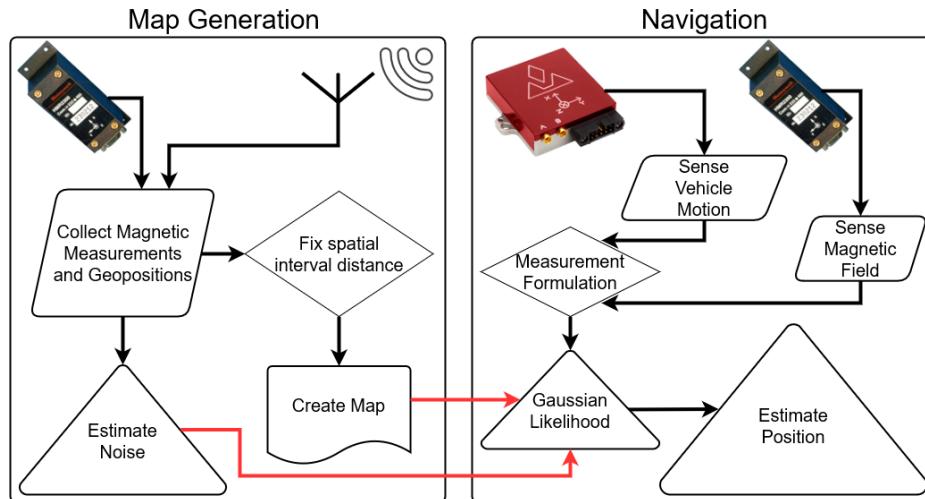
Figure 3.6: The Concept of Operations for Magnetic Map-Based Navigation.

3.3.2 Map Parameters

Maps were defined in the 'East-North-Up' local navigation frame, with the reference position $(0, 0, 0)$ located at an arbitrary point near a univeristy research building in Opelika, Alabama, matching the geodetic coordinates $32.5955°$ North, $85.2955°$ West, and 152.25 meters Up. 'Map' data sets were fixed by interpolation to a distance interval of 1.0 meter between points and were segmented. 'Navigation' data sets were instead fixed by time to a time step of 0.0333 seconds, or 30 Hertz. All relevant signal data for both map and navigation data sets were appropriately fixed to match the distance or time interval.

Maps were also sectioned such that map and navigation sets both represented one complete circuit of the route of interest. However, the same laps were not utilized for map and navigation sets. This was done to reflect real-world use cases in which temporal variations and piloting inconsistencies may affect the outcome of the navgation system.

The 'up' direction was deliberately neglected in the map and navigation data sets. This was done because solutions in the up direction provides relatively little value to ground-vehicle operators who are typically constrained to surface routes. For navigation purposes, the measurements recorded by the inertial measurement unit are transformed such that the quantities represent the approximate linear acceleration and angular velocity of the vehicle with respect to the inertial frame, resolved in the vehicle frame. This means we can approximate the forward, lateral, and vertical accelerations of the vehicle, as well as its yaw rate, pitch rate, and roll rate.

21

This was accomplished by the following euler angles:

$$\psi = 90^\circ_{IMU} \quad \theta = 0^\circ_{IMU} \quad \phi = 180^\circ_{IMU} \tag{3.1}$$

Measurements recorded by the magnetometer were also transformed to be resolved in the vehicle frame, to allow for easy calculation of the magnetic heading of the vehicle:

$$\psi = -90^\circ_{Mag} \quad \theta = 0^\circ_{Mag} \quad \phi = 0^\circ_{Mag} \tag{3.2}$$

The IMU and magnetometer sensor frames are illustrated in Figure 3.7 Measurements by the
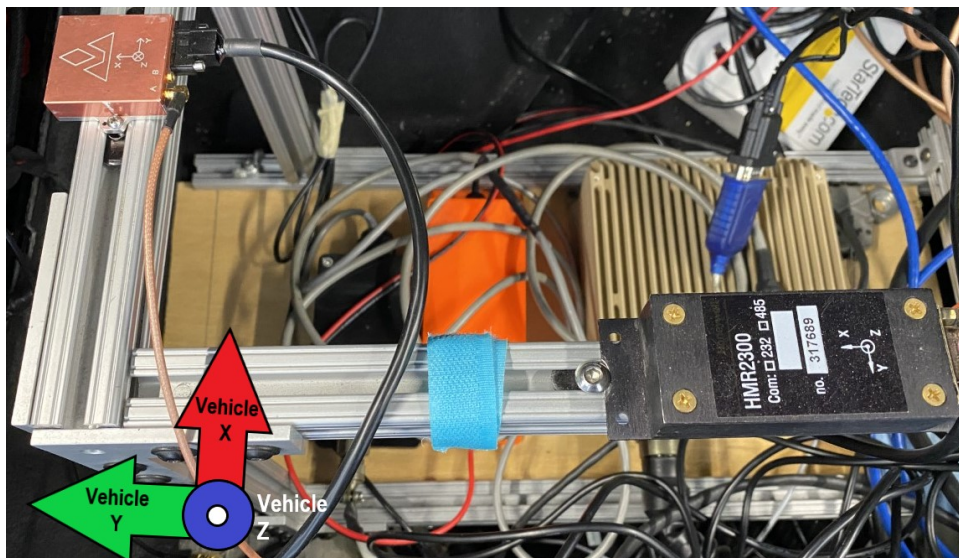
Figure 3.7: Sensor Frames: IMU (left) and Magnetometer (right). The approximate vehicle frame has been superimposed in the bottom-left.

wheel-speed encoder are recorded in the vehicle frame and need only be transformed into the navigation frame.

To avoid redundant data and ensure a consistent operating signal, both the map data set and the navigation data set are linearly interpolated. Every map data set was interpolated with respect to distance; specifically, each point on the map was defined to be an approximate distance of one meter from its neighboring points. Longer spacing intervals were previously investigated by Shockley & Raquet [14], but the 1-meter interval was determined to be an effective compromise in spatial resolution and memory requirements and this determination has carried

over to this work. The navigation data set was instead interpolated with respect to time using an arbitrary artificial sampling frequency. This thesis employed a sampling rate of 30 Hz in navigation data for time step between measurements of about 0.333 seconds. This rate was chosen to provide adquate coverage of vehicle trajectory without requiring extensive interpolants that may affect the veracity of the signal.

3.3.3   Magnetometer Calibration

Magnetometers also feature error inherent to the sensor; however, the error behavior of a magnetometer is different than an inertial measurement unit or a rotary encoder. The error model of a magnetometer is shown in equation 3.3 in which $\tilde{m}$ is the sensed magnetic measurement; S is the soft-iron disturbance manifesting as a scale factor on m, the true value of the magnetic field, b is the hard-iron disturbance manifesting as a bias on the scaled magnetic field, and η is a Gaussian noise term. [26].

$$\tilde{m} = S(m) + b + \eta(t) \tag{3.3}$$

To correct for the bias terms, a compensation term m_c can be developed and applied to the data which approximately returns it to the shape of a circle centered and the origin:

$$m_c = S^{-1}(\tilde{m} - b) \tag{3.4}$$

A sample calibration data set will allow us to estimate values of b and S. For a given location, the direction and intensity of the magnetic field will be nearly fixed, and data collected about a center rotation point will allow us evaluate the hard iron and soft iron error terms.

For this research, the calibration data set was collected at a roundabout near the VCOM route location. The roundabout was driven in nearly a perfect circle and limited to one lap for the calibration step. This location is shown in figure 3.8 and the path driven is highlighted in red. A more robust calibration implementation would also collect data about the vehicle's x-axis (roll) and y-axis (pitch); however, it was determined that these aspects may be reasonably neglected since the corresponding dynamics are only lightly present in the mapping and navigation data sets. The impact of the bias term and scale factor on the magnetic signal can be

Figure 3.8: Calibration Data Location

interpreted using an ellipsoid in which the hard-iron bias shifts the center of the magnetometer and the soft-iron bias changes the axes lengths of the ellipse.

Figure 3.9 shows the calibration data applied to itself. Since the original data collection was about the vehicle z-axis in nearly a perfect circle, we can expect an even distribution of magnetic readings in which the radius of the circle is the intensity of the field. In the uncalibrated set, the soft-iron bias is not very strong but the hard-iron bias is evident, particularly in the vehicle's lateral direction (the Y-axis). After calibration, the circular shape is maintained and the plot is nearly centered at the origin.
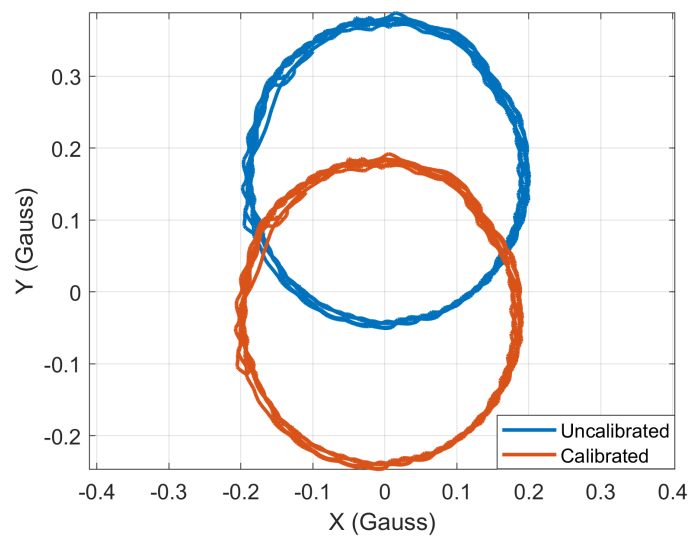
Figure 3.9: Magnetic Calibration: Roundabout

Figure 3.10 shows the same uncalibrated and calibrated data sets now applied to the VCOM route. In this case, because the path driven was not an exact circle but instead followed a set of roads around the area, we should not expect an exact circle. Sections in which the signal appears to 'bunch up' indicate noise, a dynamic disturbance, or possibly a magnetic feature in the signal.

Figure 3.11 shows the uncalibrated and calibrated data sets for the Eastside route location. These sets show the most variability, particularly in magnetic field strength. Because these plots represent multiple laps, it is suggested that only some laps were appropriate for generating mapping and navigation data sets.
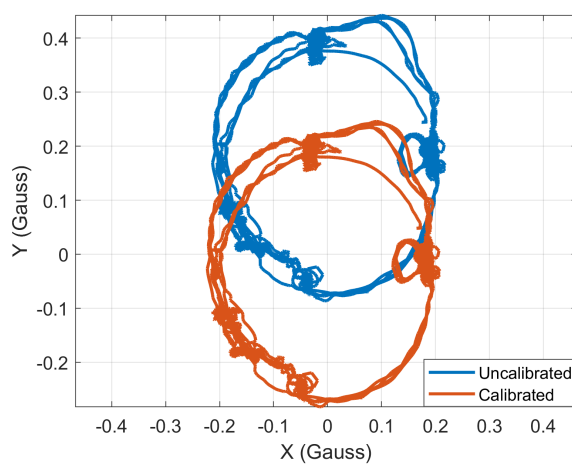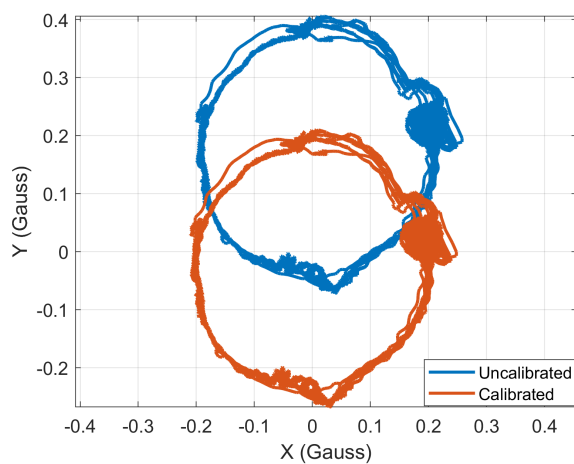
Figure 3.10: VCOM: Magnetic Calibration   Figure 3.11: Eastside: Magnetic Calibration

In each of the calibration plots, the uncalibrated data displays a noticeable hard iron bias exhibited by the shapes being centered at a location other than the origin. Each of the calibrated sets are much closer in shape and location to a perfect circle than their corresponding uncalibrated set, but some residual bias remains in each. The nature and origin of this bias is uncertain. The plots show data uncalibrated and uncalibrated from all laps of a data collection event; therefore, it is at least encouraging that this bias is consistent and repeatable.

The residual bias in the data was not expected to have negatively affected the use of magnetometer data for positioning; however, it may have introduced a small, persistent error in magnetometer heading estimates.
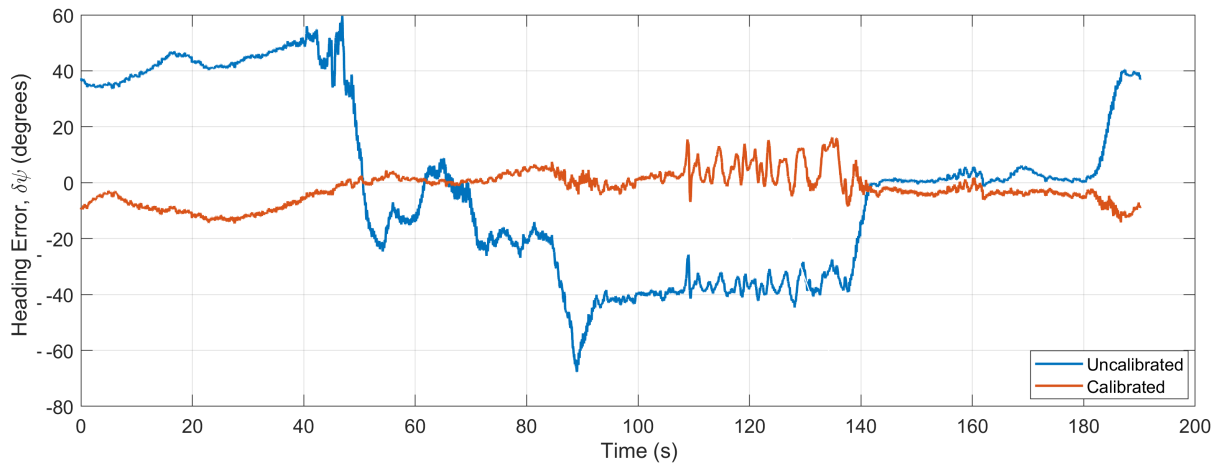
Figure 3.12: Calibration significantly reduced error in the heading estimates.

Figure 3.12 shows the error in the vehicle heading as calculated by uncalibrate and calibrated magnetometer data. Additionally, noise is still evident in the signal at certain times due to perturbations in the external environment that was traversed.

Chapter 4

Localization by Dead Reckoning

Dead reckoning was the first navigation method investigated. Dead reckoning is a simple and established means of navigation that serves as a baseline for further performance comparisons. Modern ground vehicles are standard equipped with a wide breadth of motion-sensing instruments that can be adapted for mechanization, so this method can be considered the 'default,' worst case performance conditions.

4.1   Methods

Dead reckoning was accomplished using an odometry model in which the forward velocity of the vehicle was estimated by the rotation rate of the wheels and the heading was determined using either the gyroscope or the magnetometer measurements. The state was defined to represent the position of the vehicle in the navigation frame, the velocity of the vehicle in the vehicle frame, and the heading of the vehicle with respect to the East direction:

$$\boldsymbol{x} = \begin{bmatrix} \boldsymbol{p} & \boldsymbol{v} & \psi \end{bmatrix} \tag{4.1}$$

$$\boldsymbol{p}^+ = \boldsymbol{p}^- + \tilde{\boldsymbol{v}}\Delta t \tag{4.2}$$

$$\tilde{\boldsymbol{v}} = C_V^N \boldsymbol{v} \tag{4.3}$$

Roll and pitch were neglected in these navigation solutions for the same reasons that the 'up' position was neglected. This simplified the heading update and the rotation matrix accordingly:

$$C_V^N = \begin{bmatrix} \cos(\psi) & -\sin(\psi) \\ \sin(\psi) & \cos(\psi) \end{bmatrix} \tag{4.4}$$

The yaw rate measurements provided by the gyroscope were used to update the heading of the vehicle at each time step:

$$\psi^+ = \psi^- + \dot{\psi}\Delta t \tag{4.5}$$

An alternative implementation was also developed which used the magnetometer to determine the heading of the vehicle at each point in time given the magnetic field strength measurements in the forward and lateral directions of the vehicle frame, B_x and B_y, respectively:

$$\psi = -\arctan 2(B_y, B_x) + \frac{\pi}{2} - D \tag{4.6}$$

In equation 4.6, the trigonometric function 'arctan2' was used to account for the quadrant of the heading by considering the signs of both B_y and B_x. The geomagnetic field aligns towards the magnetic north pole, so the inverse trigonometric function will provide a heading estimate measured clockwise with respect to the *magnetic north* direction. The negative sign and the term $\frac{\pi}{2}$ transform the heading solution to be defined counter-clockwise with respect to the east direction. Since the navigation frame was defined with respect to geographic true north, D in equation 4.6 refers to the declination angle and is included to correct for the relative angular difference between the geographic and magnetic north poles. This angle was evaluated according to the World Magnetic Model declination value at the initialization point and was assumed constant for the duration of each navigation attempt. In reality, D will vary with the vehicle's location about and above earth; however, the variation within the limited areas traversed is small enough that this variation could be sufficiently neglected.

4.2 Results

Figure 4.1 shows an example of dead-reckoned position solutions about the VCOM location, a 0.96 mile (1542.3 meters) route traversed in just over 190 seconds of driving. The blue line indicates the positions as provided by GPS solutions and are taken to be the true location of the vehicle at every moment in time.

Figure 4.1: VCOM Route: The vehicle's true trajectory (blue), the position as dead reckoned by wheel speed and magnetometer heading estimates (red), and the position as dead reckoned by wheel speed and gyroscope heading estimates (green).

The red line displays the positions as provided by a dead-reckoned wheel speed sensor combined with a magnetometer-derived heading estimate. The magnetic heading utilized in this solution was corrected using the declination provided by the world magnetic model at the true starting point for the dataset.

The magnetically-derived heading does not demonstrate error growth with respect to time, but an approximately-constant bias is evident in the solution which directly affects the position estimation. In the previous chapter, we found that the calibrated magnetic data still exhibited a small residual bias. Since the magnetic heading is a function of the *ratio* between the forward and lateral magnetic measurements, this bias does not manifest along the entirey trajectory

29

solution. Nevertheless, it does impact the southwest curve of the route, causing the overall trajectory to overshoot the northwest corner. Although the northern and eastern road segments show courses that are much closer to the true course of the vehicle, the early bias was enough to throw off the integrated position solution. The residual bias could be a result of internal sensor defects, unknown environmental factors inside or outside the vehicle such as electronic interference, or a mistake or oversight in the calibration procedure of the sensor measurements. The solution provided by the magnetometer-based mechanization featured a maximum position error of 84.5 meters and a maximum heading error of 16.2 degrees.

The green line shows the positions as provided by a dead-reckoned wheel speed sensor with an integrated gyroscope for heading updates. Unlike the magnetometer-based heading solution, the gyro degrades quickly over time, resulting in a position and heading that are wildly different from the true trajectory. The gyro-based mechanization furnished a maximum position error of 235.8 meters and a maximum heading error of 59.8 degrees. Figure 4.2 shows the position errors over time for each mechanization type and figure 4.3 shows the heading errors. The bias in the gyroscope measurements is plain to see by the constant slope as the heading estimates worsen with time. Both heading estimates show noise in their estimates, but the magnetic heading is additionally affected by environmental factors which cause the heading estimates to oscillate strongly between about 110 and 140 seconds along the navigation attempt.
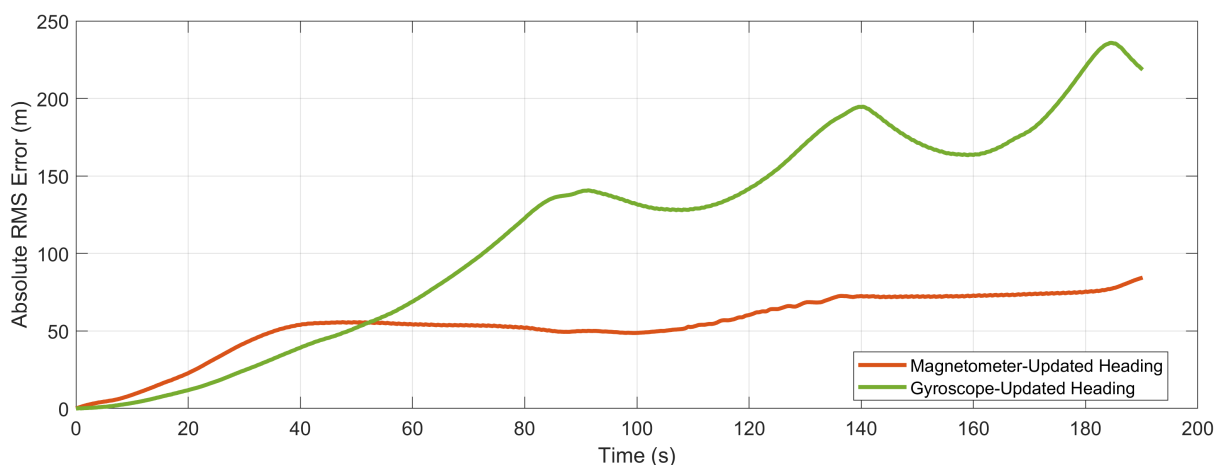
Figure 4.2: VCOM Route: Position errors over time for the magnetometer-updated and gyroscope-updated mechanization solutions in red and green, respectively.
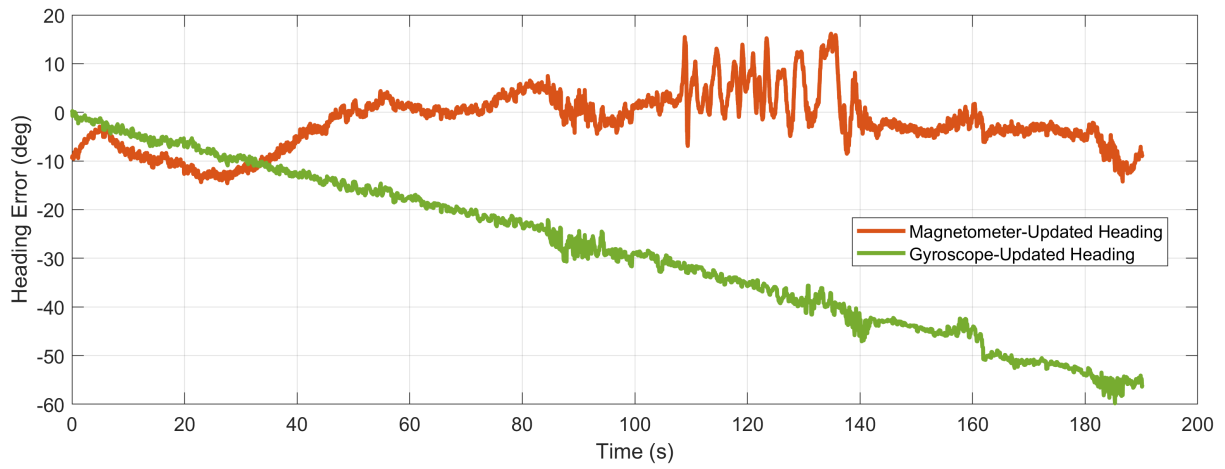
Figure 4.3: VCOM Route: Heading errors over time for the magnetometer-updated and gyroscope-updated mechanization solutions in red and green, respectively.
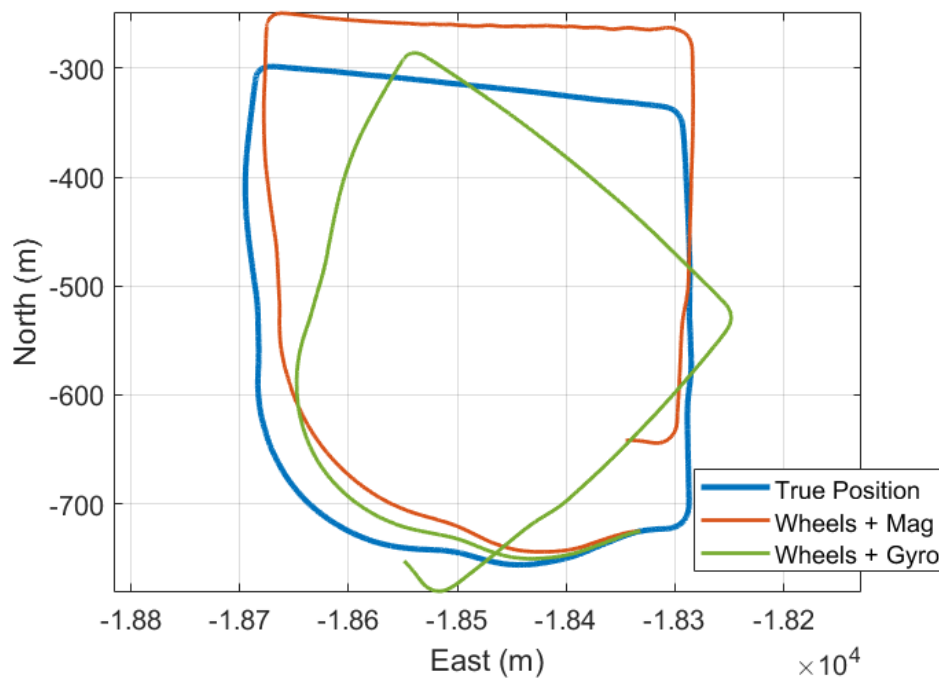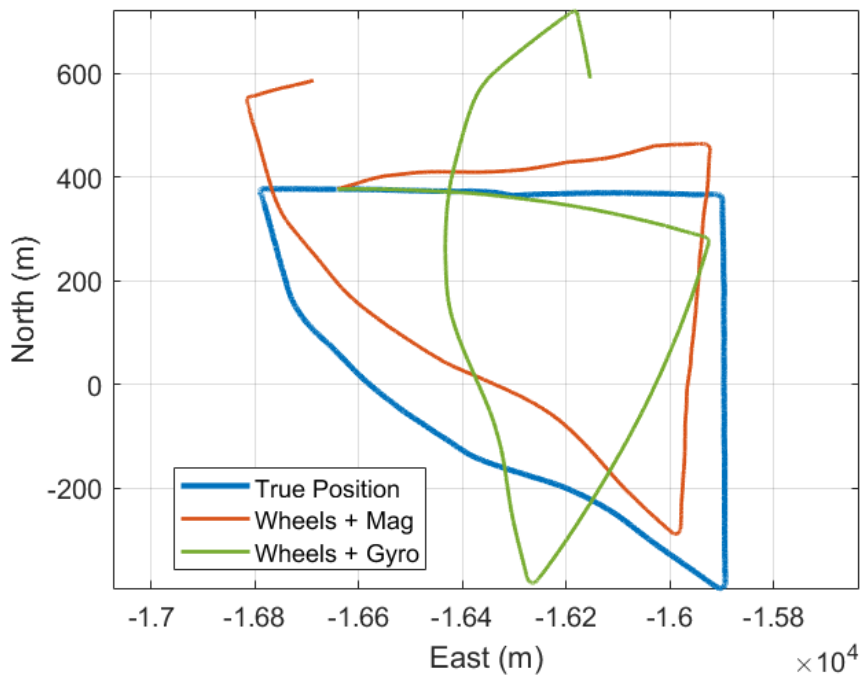

Figure 4.4: Eastside Route: The vehicle's true trajectory (blue), the position as dead reckoned by wheel speed and magnetometer heading estimates (red), and the position as dead reckoned by wheel speed and gyroscope heading estimates (green).
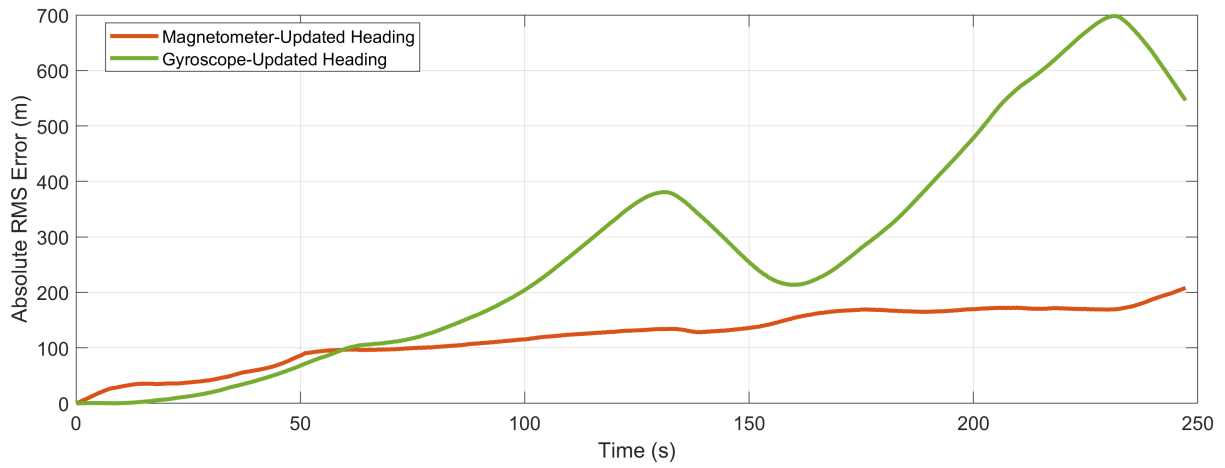
Figure 4.5: Eastside Route: Position errors over time for the magnetometer-updated and gyroscope-updated mechanization solutions in red and green, respectively.
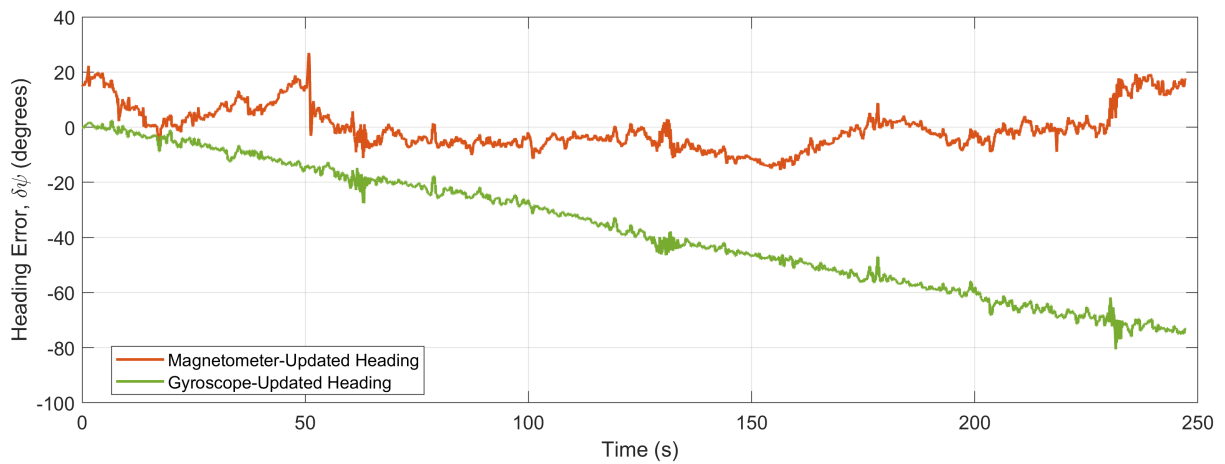
Figure 4.6: Eastside Route: Heading errors over time for the magnetometer-updated and gyroscope-updated mechanization solutions in red and green, respectively.

Chapter 5

Magnetic Map Navigation

The alternative method of navigation of interest to this thesis is magnetic map-based navigation. Using this approach, magnetic measurements from a 'Navigation' set are compared to each point of a 'Map' set and a likelihood distribution is compiled.

5.1 Method

The multivariate Gaussian likelihood function is used to compare two data points, z and $\hat{z}$, given that the measurement variance is the same in each axis [27]:

$$L_z = \beta \exp\left(-\frac{1}{2\sigma_z^2}[z - \hat{z}][z - \hat{z}]^T \right) \tag{5.1}$$

$$\beta = \frac{1}{\sqrt{(2\pi\sigma_z^2)^N}} \tag{5.2}$$

where N is the dimension of the measurement and estimated measurement vectors, z and $\hat{z}$, respectively. This equation computes a scalar value and is used to assess several possible likelihood terms. The term σ_z is derived from the modeled noise behavior of the measurement being evaluated.

In the case of magnetic map matching, z is taken to be a magnetic measurement of the nagivation set at a given point in time and $\hat{z}$ is taken to be the magnetic measurement at a point on the map. The likelihood L is calculated for every point on the map for the given navigation measurement.

5.2 Results

Figure 5.1 shows two excerpts of matching performed along the VCOM route. To achieve a position estimate, the likelihood of the three-dimensional magnetic measurement at the true location of the vehicle point is compared to every magnetic measurement belonging to the map using the multivariate Gaussian likelihood function. The normalized likelihood that each point on the map may be the vehicle's location is plotted as the blue line while the true location is marked by the red vertical line. In the first, 'unambiguous' case, the vehicle is truly located at 733.2 meters along the travelled path. The point along the map that is most-likely to be the vehicle's position based on the similarity of the corresponding magnetic measurements is also 733.2 meters along the path, indicated by the maximum value at this point. Just as importantly, almost all other points along the map were assessed to be extremely low in likelihood, reflecting a certainty that the point 733.2 meters along the track is almost certainly the vehicle's position. The only non-trivial likelihoods besides the maximum are located very close to the true vehicle location, ensuring that the position estimate will be within a small range of the truth.

In the second, 'ambiguous' case, the vehicle is truly located 1219.6 meters along the travelled path. In this case, many points along the map are similar to the magnetic measurement at the vehicle's true location as displayed by the wide range of non-zero likelihood values between about 1100 meters and 1500 meters along the route. It is also worth noting that the scale of the normalized likelihoods is smaller than in the unambiguous case by more than an order of magnitude. Because the likelihood values are normalized to sum to one, this is also a reflection of the low confidence in the estimate. This is most likely to occur along long, straight sections of a map in which the magnetic signal varies very little with distance along the road segment. These road segments are said to have insufficient *spatial frequency*. In these situations, map-matching algorithms are commonly capable of identifying which road segment the vehicle is traversing, but struggles to ascertain where *along* the road segment the vehicle may be, resulting in 'along-track error.'
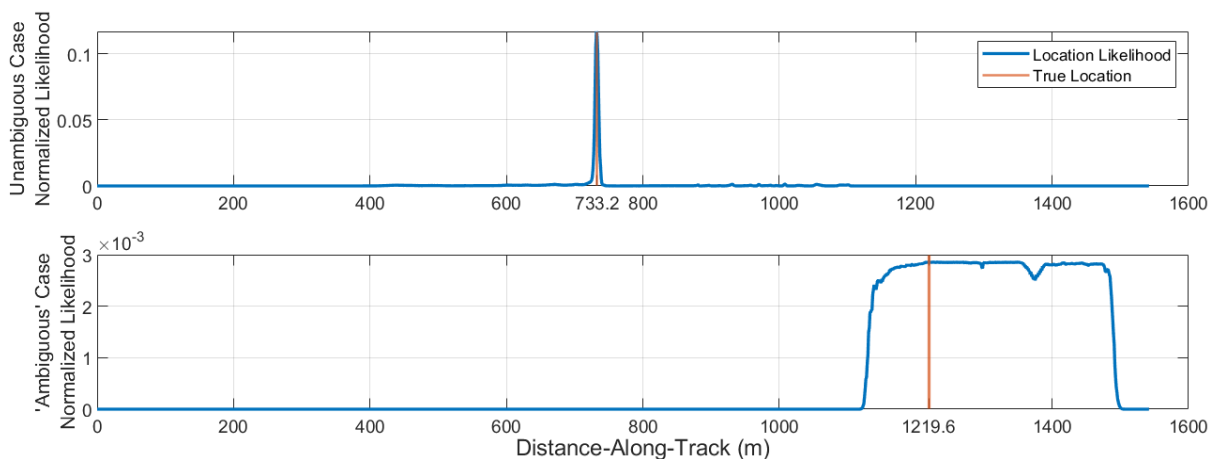
Figure 5.1: Two map-matching excerpts, in which a true position along the track is marked in red and the normalized likelihood of every point of the map along the track shown in blue.

Even if these ambiguous sections only occur intermittently, the impact on the navigation solution can be severe. Figure 5.2 shows the entire true path driven along the VCOM route along with the estimated path according to the most-likely position calculated by the multivariate Gaussian likelihood function at each time step.
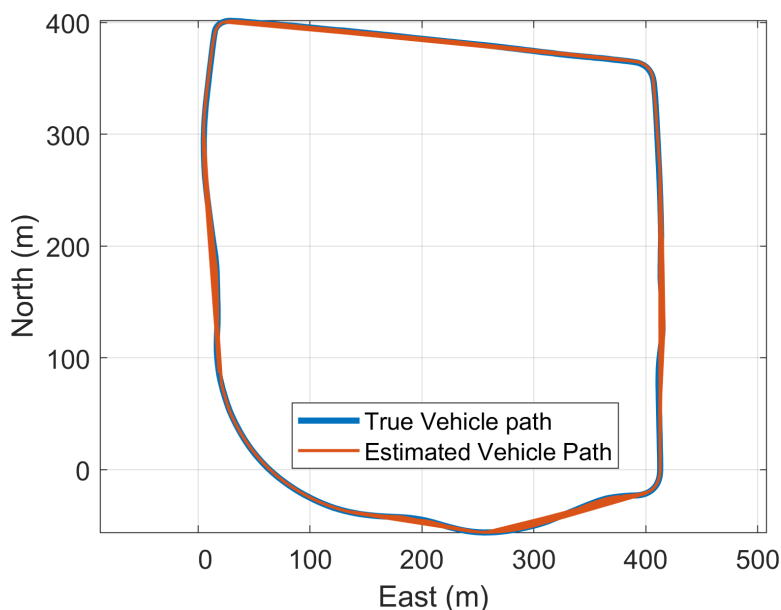
Figure 5.2: VCOM Path visualization of magnetic map-matching selecting the maximum liklelihood position.

At first, it may appear that the estimation performs adequately by following the mapped route very closely, but this is because the map-matching method can only compute solutions that are on the map. Some segments of the path appear to go off the map but this is a result

35

of sequential position estimates that are very far from one another, so the corner between them is cut. Figure 5.3 reveals that the average position error was in fact 18.7 meters and reached a maximum of 252.4 meters. Spikes in the error of over 100 meters were common along the route. Navigating by this method is unreliable and prone to discontinuities that may only amplify the position error.
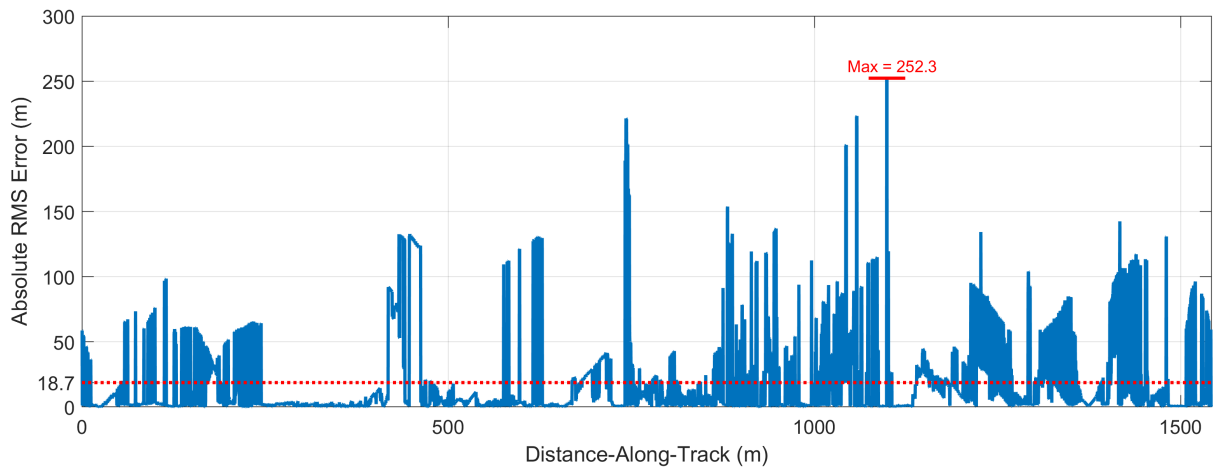
Figure 5.3: Positional error of the ma-matching method. The mean error is shown by the dashed red line and the maximum error annotated with the solid red marker.
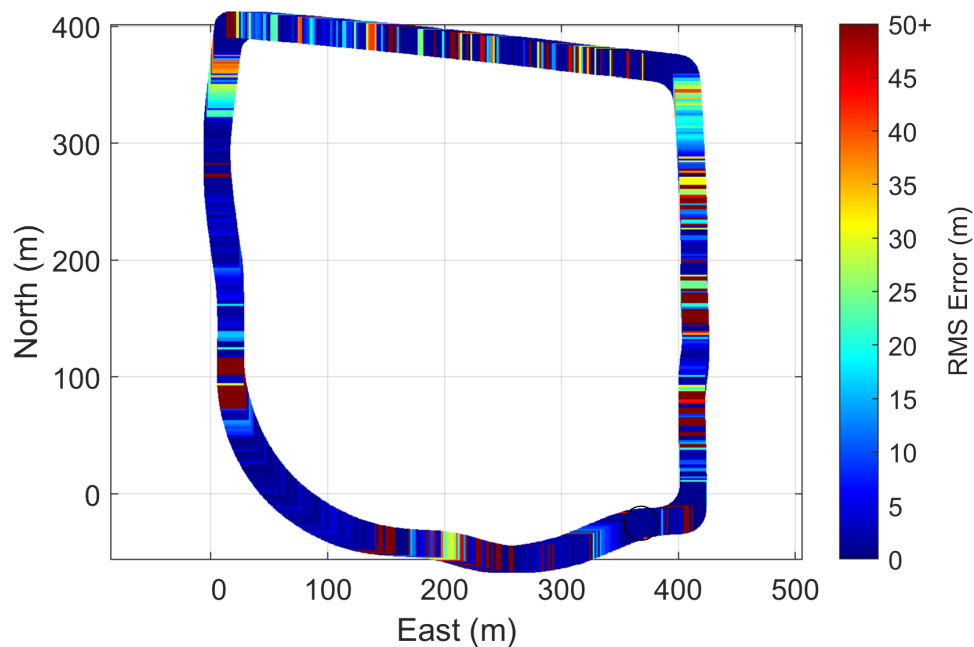
Figure 5.4: Error Color Map of the map-matching method along the VCOM route. Errors greater than 50 meters are represented by dark red.

Figure 5.4 shows the true path driven along with the positional error at every point according to the colormap shown, in which exact matches of zero meters of error are dark blue

and any poor matches of greater than 50 meters of error are dark red, with a band of colors for matching errors in between. The maximum-likelihood map-matching approach appears to be effective for certain stretches of the navigation attempt, particularly the southwest curve and western road stretching north. However, error spikes occur at seemingly random intervals and vary widely in intensity. Estimates can jump across the map immediately and return just as quickly.

Chapter 6

Magnetic Map Navigation with Vehicle Odometry

To improve the accuracy, precision, and reliability of themap-matching technique, a particle filter was developed. The particle filter, first described in 1993, applies a probabilistic approach to estimate nonlinear, non-Gaussian, and Bayesian probability processes [28]. For vehicle motion, road maps present non-Gaussian probability distributions, necessitating this style of estimator [29]. For ground-vehicle navigation, the particle filter functions as simulation-based method of representing the time evolutions of state probability distribution. This filtering framework consists of selecting a process for the evolutions to follow, called a propagation step, a likelihood assessment and measurement update step, the estimation solution, and where appropriate a re-sampling step to reduce redundancies and cull excessively low-probability simulations. Next, we will discuss each of these parts in detail.

6.1   Methods

Vehicle odometry measurements can be used to enhance the particle filter implementation by one of two approaches:

1. Augmenting propagation, in which the evolution of the particles is informed to coincide with the sensed motion of the vehicle.

2. Augmenting likelihood, in which the sensed motion of the vehicle is used to evaluate particles.

This thesis will focus on the first of these approaches.

6.1.1 Particle Definition

First, we must define the filter's constituents: the particles. The term *particle* refers to a single discrete simulated instance of the states at a given moment in time. This particle represents one possible state solution; however, multiple particles are typically implemented to account for natural and artificial noise in the system. The particles each have the same state vector structure composed of a position, velocity, and acceleration, each with an east and a north component:

$$\mathbf{x} = \begin{bmatrix} \mathbf{p} & \mathbf{v} & \mathbf{a} \end{bmatrix}^{\mathsf{T}} \tag{6.1}$$

Additionally, each particle has an assigned weight that approximately reflects its signifigance to the solution:

$$\mathbf{W} = \begin{bmatrix} w_1 \ w_2 \ \dots \ w_n \end{bmatrix} \tag{6.2}$$

These particles are initialized normally about the true starting point by some arbitrary distribution with accelerations and velocities of zero and a uniform weight distribution of $\frac{1}{n}$'. The heading, ψ may also be distributed about the true starting heading or else neglected if the propagation & likelihood functions do not make use of it.

6.1.2 Propagation

In the propagation step, the state of the particles change according to some chosen method or function. The process function, displayed in equation 6.3, consists of a state transition matrix F which applies to its previous state and an artificial noise function which is summed and shown as the matrix G. The artificial noise function serves to ensure that particles do not move in redundant or tightly correlated patterns and encourages a wider coverage of the probability distribution. Filter designers also benefit from selecting propagation functions which either change the particles' states in ways that closely simulate the actual movement of the vehicle, or else that allow the filter to efficiently assess the evolution of the particles' likelihoods.

$$\boldsymbol{x}^{+} = F\boldsymbol{x}^{-} + G \tag{6.3}$$

The most straightforward application of a particle filter to the map-matching context was pioneered by Shockley and Raquet (2014), who utilized a Gauss-Markov process to calculate the acceleration for each particle based on the velocity at the previous time step:

$$\boldsymbol{a}_k = \frac{-\boldsymbol{v}_{k-1}}{\tau} + \eta \tag{6.4}$$

where the arbitrary parameter τ is the time constant of the system, and the arbitrary parameter η is some zero-mean, Gaussian random noise value with a standard deviation of σ_{model}. To update the velocity and position values at each time step, the acceleration is integrated using the consistent time-step of the navigation data set. Therefore,

$$F = \begin{bmatrix} 1 & 0 & \Delta t & 0 & \Delta t^2 & 0 \\ 0 & 1 & 0 & \Delta t & 0 & \Delta t^2 \\ 0 & 0 & 1 & 0 & \Delta t & 0 \\ 0 & 0 & 0 & 1 & 0 & \Delta t \\ 0 & 0 & 0 & 0 & 1 & 0 \\ 0 & 0 & 0 & 0 & 0 & 1 \end{bmatrix} \tag{6.5}$$

$$G = \begin{bmatrix} 0 & 0 & 0 & 0 & \sim N(0, \sigma_{model}) & \sim N(0, \sigma_{model}) \end{bmatrix}^{\mathsf{T}} \tag{6.6}$$

Particles are not otherwise restricted in the magnitude or direction they may propagate and therefore propagate independently of one another and independently of the map. Selecting a value for σ_{model} that is within the typical range of a ground vehicle is advisable, but even a well-tuned filter will see a large number of particles move very differently than the vehicle being tracked. Particles may rapidly accelerate, decelerate, or change direction to an extent unlikely or even impossible for a ground vehicle. Therefore, it is essential to the success of the filter that a well-designed likelihood and weighting system be defined as well.

6.1.3 Weighting & Estimation

The particle filter also makes use of the multivariate Gaussian likelihood function to make quantitative comparisons between data points. Previously, this function was applied to compare a specific magnetic measurement from the navigation data set to every mapped magnetic measurement along the map data set. One innovation of the particle filter is to instead limit the search space to the areas of the map that particles have propagated to. This is done by determining the map point nearest to the particle's current position and associating the that map point's magnetic measurement with the particle. A particle's magnetic likelihood is then a function of the given navigation magnetic measurement and the magnetic measurement at the mapped point associated with it.

Even if a particle does not lie exactly on the map, a particle that is very near to a particular mapped point is sufficiently represented by the map's magnetic measurement at that point. However, this association is made regardless of the actual distance from the particle to the map point. This means particles that are very far from the actual map may associate with map measurements that evaluate very highly in likelihood and can inadvertently produce solutions that are very far from the mapped route. To mitigate this, a second likelihood assessment is performed to compare the navigation position of the particle to the nearest point on the map in the navigation frame. The multivariate Gaussian likelihood function is again employed for this purpose with z being the position of the particle in the east and north directions and $\hat{z}$ being the position of the nearest mapped point, also in the east and north directions, as well as the parameter σ_{map} to quantify how strongly particles should be restrained to the map. This second likelihood term is multiplied by the first likelihood term that was produced from the magnetic measurements to determine the overall likelihood of the particle. Since this second term decreases the likelihood of particles that are far from the map while only marginally affecting particles that are near to the map, this operation is referred to as a 'road deweighting' step.
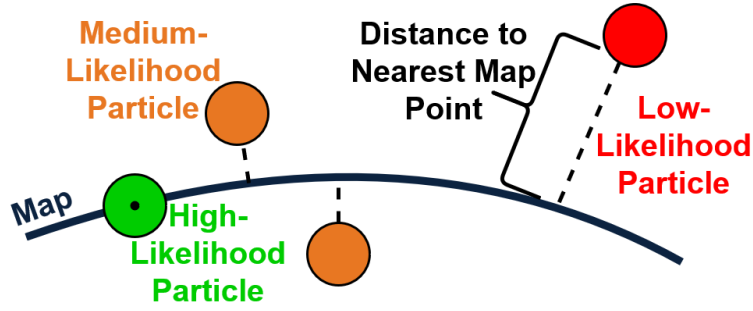
Figure 6.1: An example of road deweighting. Likelihood is inversely proportional to the distance from the map.

The weight of the particles is updated using the overall likelihood product. Typically, the likelihood product is multiplied by the previously-assessed weight values and normalized to produce a new quantity for the weight of the particle in a format called *sequential importance sampling*:

$$w_i^+ = w_i^- * \frac{\Pi_{e=1}^l L_z}{\Sigma_{i=1}^n \{ \, (\Pi_{e=1}^l L_z)(w_i^-) \, \}} \tag{6.7}$$

The navigation solution is the position provided by the weighted average of all of the particles [30]:

$$\bar{x} = \Sigma_{i=1}^n w_i x_i \tag{6.8}$$

Although this provides an estimation solution for each state variable, the only ones of interest to this research are the positions in east and north coordinates. Significantly, the solution is not constrained to the map and can provide position estimations that are not on the mapped path.

6.1.4   Resampling & Solution Stability

Commonly, particle filters employ a resampling step to ensure the filter does not continue to propagate large numbers of particles with exceedingly low likelihoods. For this filter, resampling with replacement is carried out whenever the effective sample size of the particles falls below an arbitrary, user-defined threshold value. The effective sample size estimates the number of particles whose weights contribute meaningfully to the total likelihood of the distribution:

$$n_{eff} = \frac{1}{\Sigma_{i=1}^n w_i^2} \tag{6.9}$$

If a small number of particles hold the majority of the probability distribution of the particle set, systematic resampling with replacement, or 'bootstrapping,' probabilistically replaces low-likelihood particles with duplicates of higher-likelihood particles [31]. Because particles propagate independently of one another and some random noise term is included in every propagation method investigated, these duplicate particles will almost certainly deviate in subsequent time steps, so particles do not become redundant.

6.2 Gauss-Markov Propagation

The following particle filter standard parameter list was established for performance evaluation:

Particle Filter Parameters: 'Standard' Filter

$n = 1000$ $\sigma_{map} = 6$ meters

Resampling Percentage = 50% $\sigma_{mag} = 0.05$ Gauss

Initialize about true starting point (no offset) $\sigma_{model} = 5 \, m/s^2$

$\sigma_{init} = 50$ meters $\tau = 100$ seconds

To gauge filter performance, a map data set and navigation data set were selected from different laps of the same data collection event along the same route. In this case, Lap 3 of the VCOM collection event served as the mapping data set and Lap 2 served as the navigation set. Because stochastic variables are present in the filter, particles will evolve randomly and one navigation attempt will feature slightly different error dynamics from another. The following is a representative results set, selected from fifty runs of the filter since the error dynamics of the run most closely matched the overall average of the set.

Figure 6.2 shows three position trajectories: The map in blue, the actual path driven in green, and the estiamted path driven in red. At first glance, it appears that the filter follows the map and true trajectory rather well, evidenced by the estimated path closely layering on top of the true path. However, path visualization can be a misleading indicator of performance. Although the estimated path of the vehicle appears to align with the mapped and true paths, the filter suffered from the problem of 'along-track' error. These errors are more evident in
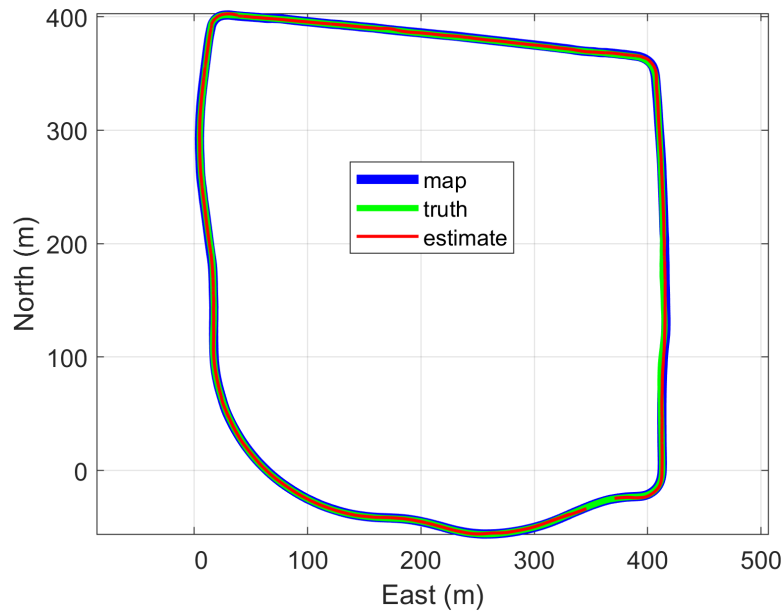
Figure 6.2: VCOM with Gauss-Markov Propagation: Path Visualization.

figures 6.3 and 6.4. The former image shows the RMS error over distance travelled (by the true path) as the blue line, with the dashed red line showing the average error and the solid red marker indicating the maximum error and its location along the track. The green dashed line reflects the standard deviation of the particle spread. The latter image charts the RMS errors at nearly every point along the true path driven using an associated color map beginning and zero and maxing out at 50 meters of error. Clearly, the filter did perform well for large portions of the map, but also struggled significantly in the northwest corner and eastern straight-away. Most likely, during these sections the spatial frequency of the magnetic signal was reduced, leading to many ambiguously likely particle positions along the road and uncertainty in the filter solution. These route segments featuring higher error also correspond to the moments in which the standard deviation of the particle spread is greatest, indicating a large range positions were considered reasonably possible by the filter.
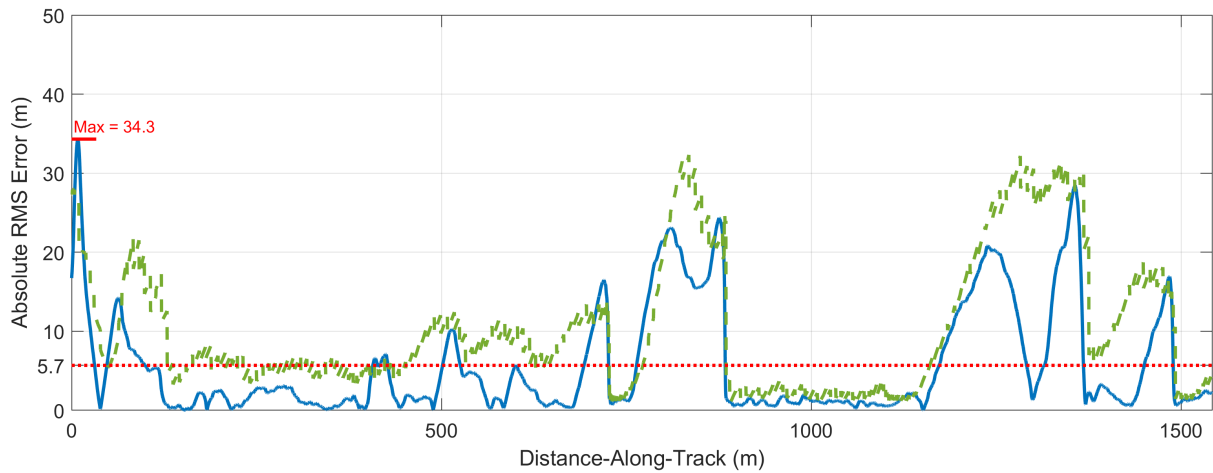
Figure 6.3: VCOM with Gauss-Markov Propagation: Error along track, with average error shown by the dashed red line, max error by the annotation and solid marker, and deviation of the particle spread by the dashed green line.
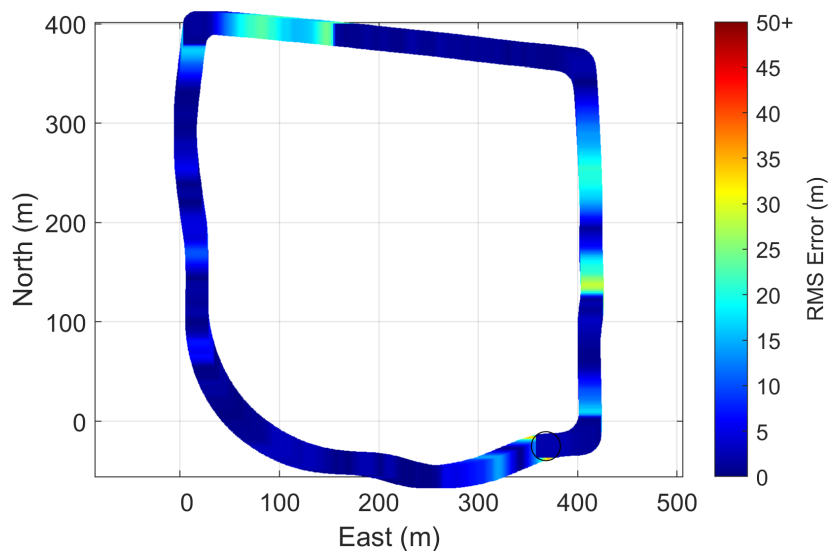
Figure 6.4: VCOM with Gauss-Markov Propagation: Error Color Map.

6.3 Wheel-Speed & Magnetometer-Heading Propagation

Because the performance of the particle filter is dependent on the evolution of the particles' states over time, developing a particle propagation model that more closely aligns with the motion of the vehicle should allow for more high-likelihood particles and produce a more accurate solution. The first such implementation explored in this research was the application of a wheel-speed sensor to provide linear movement information and the magnetometer measurements for heading estimation. Normally, this use of magnetometer data twice in the same filter would be a poor choice of implementation, as it would require use of the same information

45

to perform process and measurement updates. However, because we are applying the magnetometer data first to update the *heading* of the particles and then secondly to assess the *position* of the particles, the data is not applied in a redundant manner.

To utilize these sensors in the propagation function of the particles, the particle state is redefined to match the definition used by the dead-reckoning implementation in equation 4.1 introduced in chapter 4: we will again make use of the heading variable, ψ, but because wheel-speed encoders are used to estimate the vehicle velocity, the acceleration variables $\boldsymbol{a}$ are unnecessary and are removed.

At each time step, the position of each particle evolves according to the vehicle velocity estimate modified by an artificial Guassian noise term η_v after it is transformed into the navigation frame using the modified heading angle $\tilde{\psi}$.

$$\boldsymbol{p}^+ = \boldsymbol{p}^- + \tilde{\boldsymbol{v}}\Delta t \tag{6.10}$$

$$\tilde{\boldsymbol{v}} = \tilde{C}_V^N \boldsymbol{v} + \eta_v \tag{6.11}$$

$$\tilde{C}_V^N = \begin{bmatrix} \cos(\tilde{\psi}) & -\sin(\tilde{\psi}) \\ \sin(\tilde{\psi}) & \cos(\tilde{\psi}) \end{bmatrix} \tag{6.12}$$

The modified heading $\tilde{\psi}$ is calculated for each particle using the heading calculation provided by equation 4.6, but each component of the magnetometer measurement is altered by a Gaussian noise term.

$$\tilde{\psi} = -\arctan 2(\tilde{B}_y, \tilde{B}_x) + \frac{\pi}{2} - D \tag{6.13}$$

$$\tilde{B}_x = B_x + \eta_{B_x}$$
$$\tilde{B}_y = B_y + \eta_{B_y} \tag{6.14}$$

To facilitate the above propagation approach, the filter requires users to provide two additional parameter values:

Additional Parameters: Wheel-Speed + Mag-Heading Filter

$\sigma_{initial\ heading} = 20°$ $\qquad\qquad\qquad\qquad$ $\sigma_{mag\ heading} = 0.05$ Gauss

The parameter $\sigma_{initial\,heading}$ describes the Gaussian distribution of the initial heading of the particles about the true heading of the vehicle. The parameter $\sigma_{mag\,heading}$ describes the Gaussian noise added by the filter to each component of the magnetic measurement, η_{B_x} and η_{B_y}, for the purposes of heading estimation. This variable is distinct from σ_{mag} which is used in the likelihood evaluation step. The previously defined parameter σ_{model} is also used to adjust the velocity measurement by a random Gaussian value, η_v. These artificial noise terms are incorporated so that particles do not move in parallel paths, which would result in redundant calculations and gaps in the search space. These new parameters are used in conjunction with the values supplied in the previous section.

The paths mapped, driven, and estimated are shown in figure 6.5.
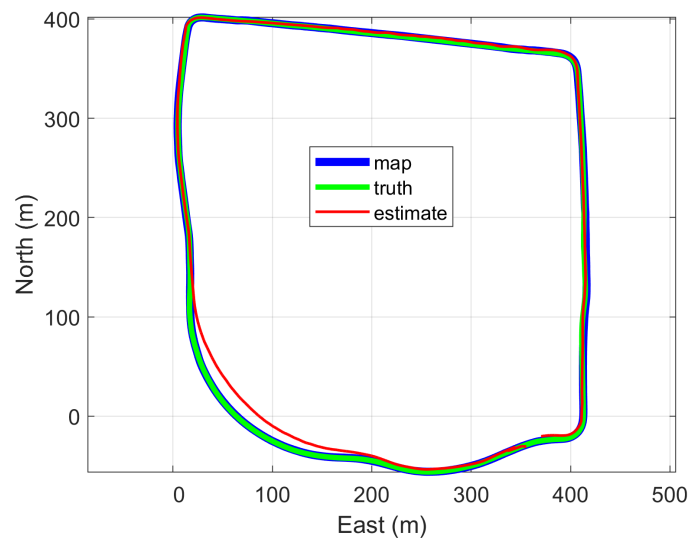
Figure 6.5: VCOM with Wheel-Speed & Magnetometer-Heading: Path Visualization.

Immediately visible is the estimation's brief disengagement from the mapped path not long after the beginning of the navigation attempt. This diversion corresponds with the shortened southwestern curve seen in the dead reckoning implementation. However, unlike the dead reckoned path estimate, the particle filter succesfully corrects for this diversion, returns to the mapped path, and even catches up with the vehicle as it traverses further along the path.

During the diversion, each of the particles propagate according to the magnetometer-derived heading estimate, but an error in this estimate causes the particles to propagate away

from the map. Normally, the road deweighting step would strongly encourage particles to remain near to the map by reducing the likelihood of particles located away from the map; however, because all of the particles propagate along a path that parallels the map and at roughly an equal distance from the map, every particle is associated with a highly-weighted map measurement and deweighted by nearly the same factor, resulting in the perpetuation of a solution not on the map. A more precisely tuned filter may reduce the effect of this phenomenon.
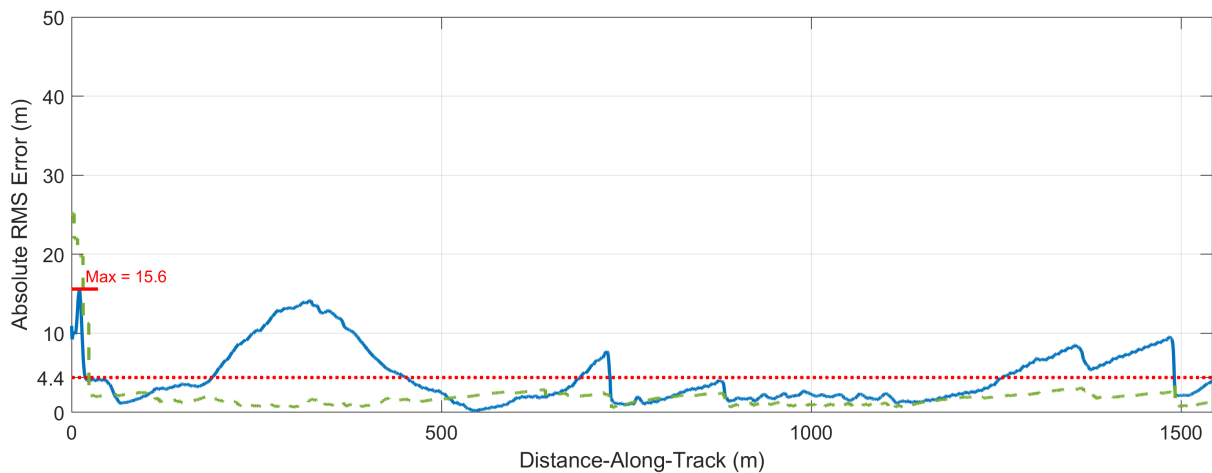

Figure 6.6: VCOM with Wheel-Speed and Magnetometer-Heading: Error along track, with average error shown by the dashed red line, max error by the annotation and solid marker, and deviation of the particle spread by the dashed green line.

Figure 6.6 shows the error dynamics along the track. The average error is reduced by 22.6% from the Gauss-Markov propagation implementation and the maxmimum error is reduced by 54.3%. The standard deviation of the particle spread is also greatly reduced, often achieving a smaller positional range than the error. In figure 6.7, the diversion is visible as the light blue segment in the bottom-left corner, but the locations in the northwestern and eastern segments that the Gauss-Markov implementation struggled with are significantly improved.
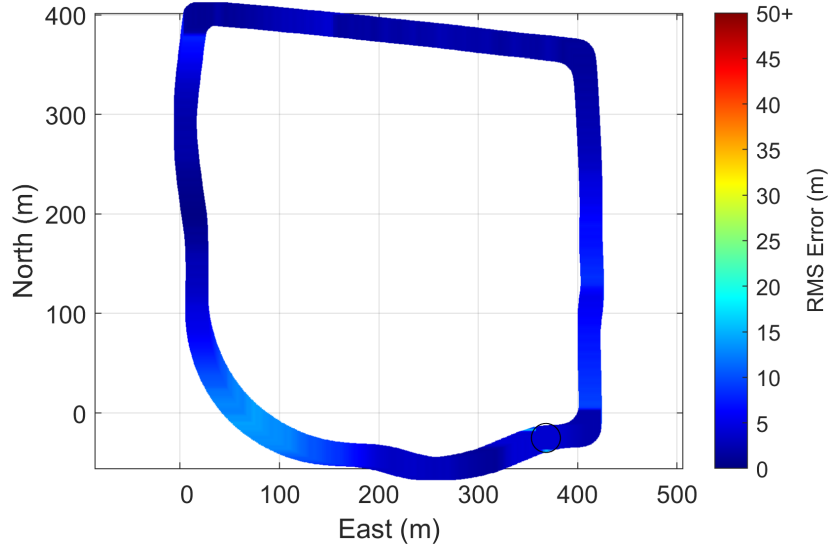
Figure 6.7: VCOM with Wheel-Speed and Magnetometer-Heading: Error Color Map.

6.4 Wheel-Speed & Gyroscope-Heading Propagation

For the gyroscope-updated heading filter, the same particle definition may be used as for the magnetometer-updated heading filter. The position again updates using the transformed and modified velocity estimate, but the heading is instead updated according to a modified yaw rate signal, $\tilde{\dot{\psi}}$:

$$\tilde{\dot{\psi}} = \dot{\psi} + \eta_{\dot{\psi}} \tag{6.15}$$

$$\psi^+ = \psi^- + \tilde{\dot{\psi}}\Delta t \tag{6.16}$$

One additional parameter is defined:

Additional Parameter: Wheel-Speed + Gyro-Heading Filter

$$\sigma_{gyro\,heading} = 3\,\tfrac{deg}{sec}$$

This parameter describes the random Gaussian noise that is added to the gyroscope measurements during the heading update of each particle.

Figure 6.10 shows the error dynamics. Although the gyroscope-updated filter shares nearly the same maximum error with the magnetometer-updated heading filter, the gyroscope-heading filter sees this error at the very beginning of the navigation attempt, suggesting that this may be a quirk of the intialization method. The second, smaller peak at about 46 meters along the track

49
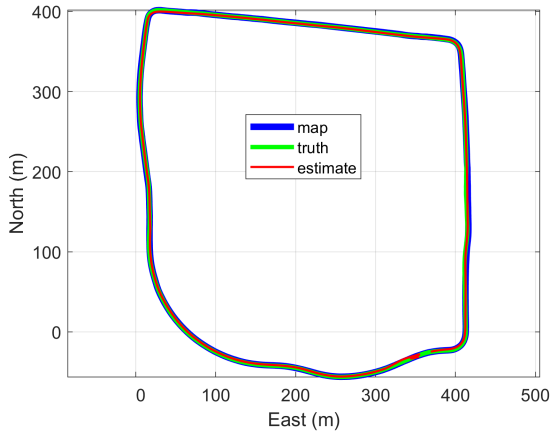
Figure 6.8: VCOM with Wheel-Speed and Gyroscope-Heading: Path Visualization.
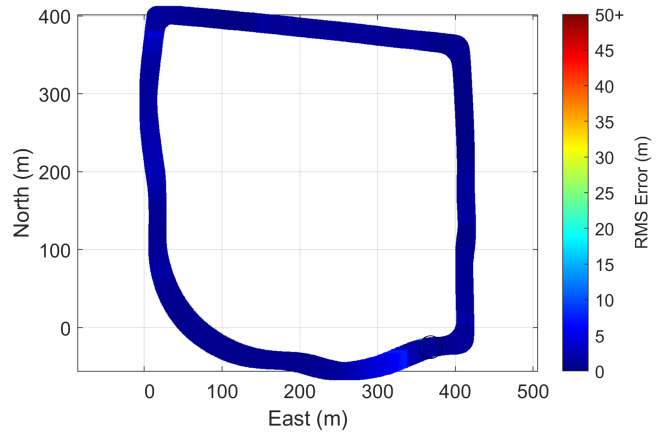
Figure 6.9: VCOM with Wheel-Speed and Gyroscope-Heading: Error Color Map.

is an RMS error value of 7.7 meters. Regardless, the average of 1.3 meters is a 69.4% decrease from the magnetometer-heading filter. Figure 6.9 shows very little color variation, indicating strong performance throughout the navigation attempt.

Figure 6.10: VCOM with Wheel-Speed and Gyroscope-Heading: Error along track, with average error shown by the dashed red line, max error by the annotation and solid marker, and deviation of the particle spread by the dashed green line.

Chapter 7

Off-Route Performance

One of the perceived drawbacks of map-based navigation is the requirement that navigators closely follow routes and paths defined by the Map. Even as small adjustment as being in the incorrect lane could potentially affect the repeatability of a magnetic signal for navigation [14].

Real-world users, however, will often experience accidental or deliberate deviations in intended routes, either due to piloting errors or changes in path accessibility due to outside factors such as road maintenance. For this reason, additional datasets have been collected in which the piloted course did not match the mapped dataset. These alternative, 'off-route' data sets were selected to illustrate the robustness of the map-based approach and currently-developed filter implementations to small and large deviations in ways that are representative of possible real-world encounters. The key questions asked in this chapter are:

1. Once the map is exited or nominal conditions are interrupted, does the filter attempt to track the vehicle off the map or stall?

2. Once the map is re-entered or nominal conditions are resumed (if they are resumed), does the filter recover a tracking solution and if so with what accuracy?

Because map-matching is only possible for points and measurements on the map, we expect the filter performance to degrade after off-route conditions are encountered. However, the vehicle odometry measurements allows for the particles to be 'steered' in the general direction of the vehicle and may provide a means to track the vehicle temporarily while magnetometer data is not usable or to reacquire a position solution once the off-route conditions end.

51

Figures 7.1 and 7.2 show the nominal performance results for the gyroscope-updated heading filter.
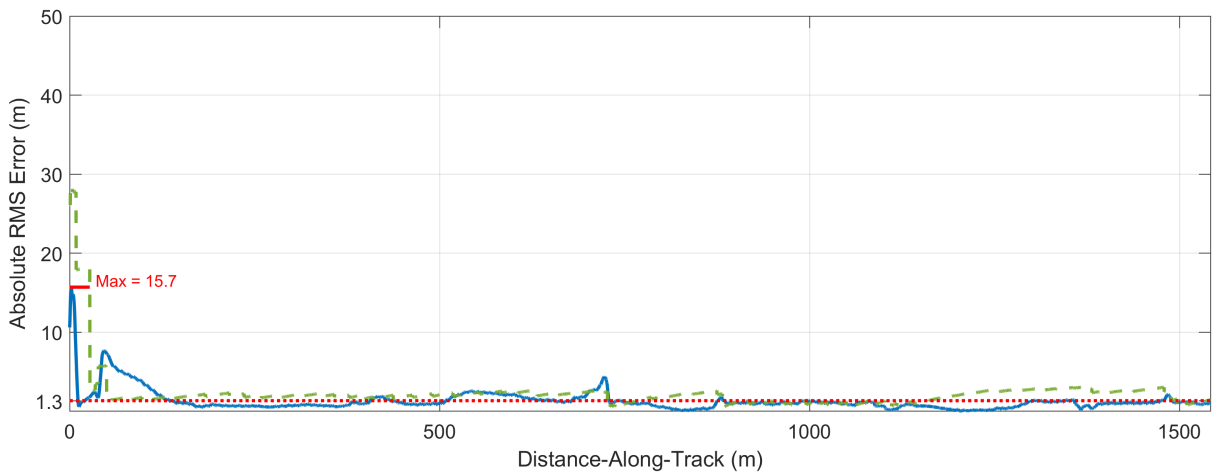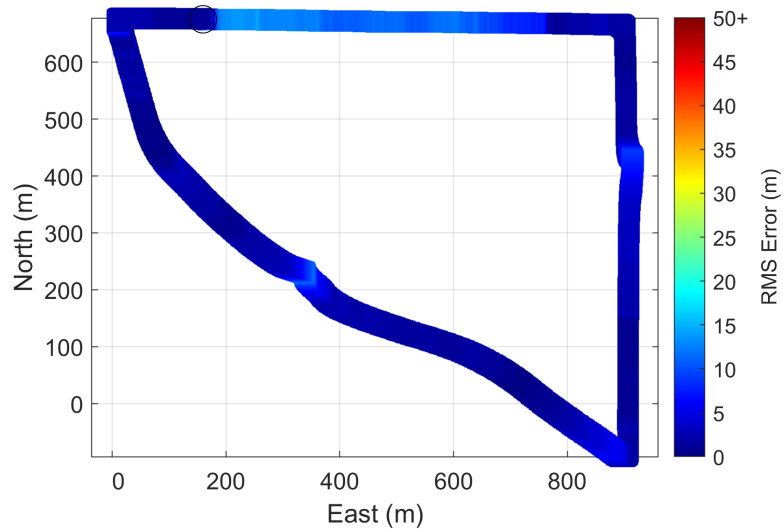

Figure 7.1: Eastside Nominal with Wheel-Speed and Gyroscope-Heading: Error Heat Map.

Figure 7.2: Eastside Nominal with Wheel-Speed and Gyroscope-Heading: Error along track, with average error shown by the dashed red line, max error by the annotation and solid marker, and deviation of the particle spread by the dashed green line.

7.1   Detour

The first additional dataset collected was titled the 'Detour' set and mostly follows the Eastside route except that the navigation attempt began and ended at a point on the eastern road segment, just after the northeast corner, and the attempt featured additional turn made onto a side road

along the final leg of the original path. Figure 7.3 shows the actual path driven during the navigation attempt.

This side road turns north before bending west to reconnect with the final segment of the route. This short deviation is approximately 494.6 meters in length and was driven in 52.83 seconds. This segment was selected for the 'detour' navigation set because it was expected that the brief time and distance to traverse would limit errors development during the off-route event. Also, since the detour segment disconnects and reconnects with the map along the same road, it was thought that particles would remain or propagate within a vicinity that would encourage reacquisition of the vehicle once the vehicle re-entered the map.

Figure 7.3: Route 'Detour,' also beginning near the northwest corner.

7.1.1 Wheel-Speed and Mag Heading

The magnetometer-updated heading filter is capable of tracking the vehicle somewhat closely for the beginning of the navigation attempt. The trajectory of the detour appears to be emulated by the particles, but the road deweighting and magnetic map-matching likelihood terms deter the particles from following a mechanization very closely. As a result, the particles and the solution remain too close to the map.

Figure 7.4: Eastside Detour with Wheel-Speed and Magnetometer-Heading: Path Visualization.

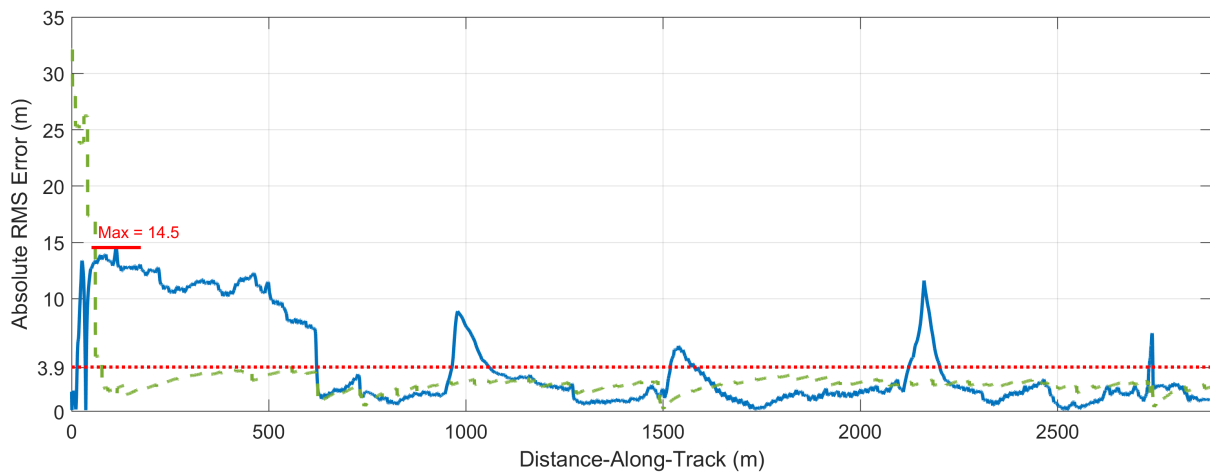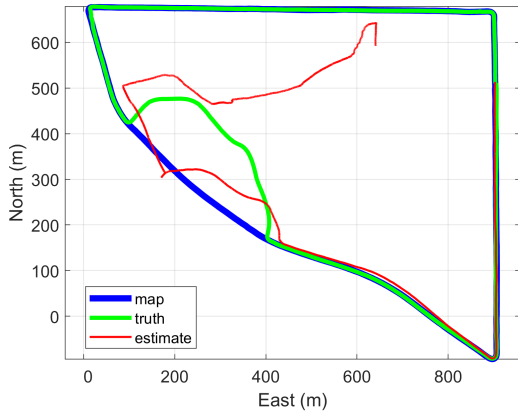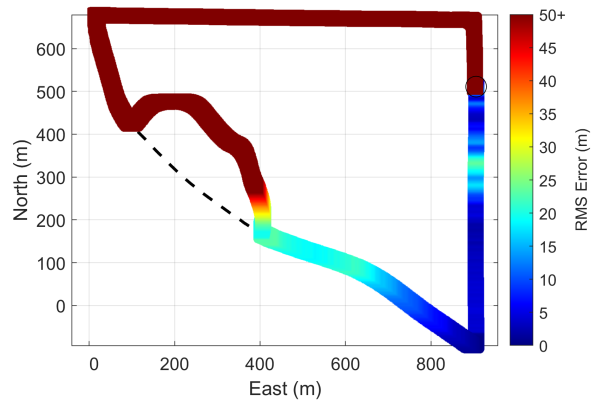Figure 7.5: Eastside Detour with Wheel-Speed and Magnetometer-Heading: Error Color Map.
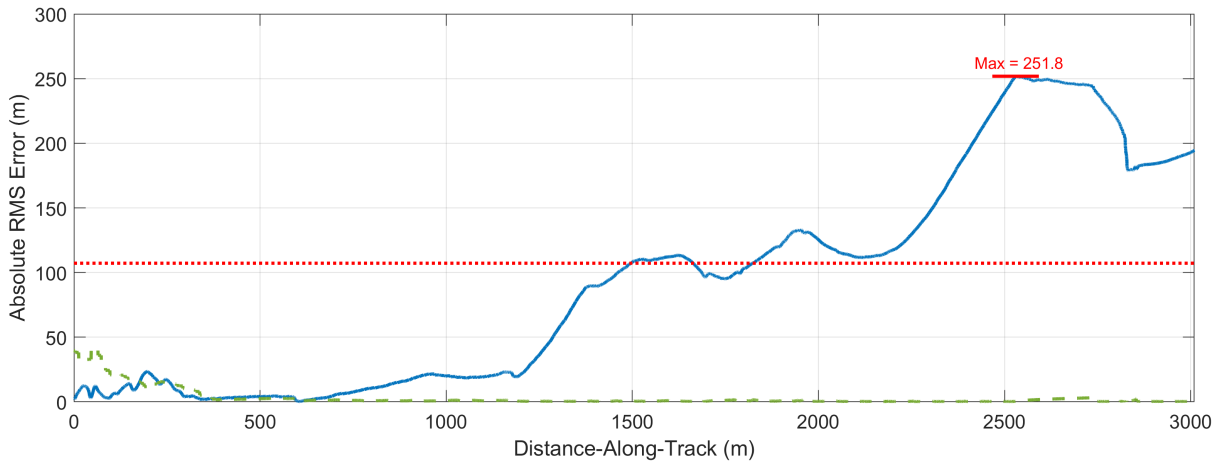

Figure 7.6: Eastside Detour with Wheel-Speed and Magnetometer-Heading: Error along track, with average error shown by the dashed red line, max error by the annotation and solid marker, and deviation of the particle spread by the dashed green line.

The green dashed line in figure 7.6 indicates that the particle spread remains very tight for the duration of the navigation attempt, reflecting a small search space of map data. This becomes a liability when the vehicle re-enters the map, as the particles continue to match the heading of the vehicle but their small spread and large distance from the true location lead to comparisons of map magnetic measurements that are very disparate from the vehicle's magnetic measurements, throwing off any possible position correction. The filter apears to recognize the northwest and northeast turns of the vehicle, but the failure of the map-matching element precludes a useable solution as the vehicle drives the remainder of the mapped route.

7.1.2 Wheel-Speed and Gyro Heading

The gyro-updated heading filter shows similar dynamics as the mag-updated heading filter before and during the off-route event. It also fails to reconverge after the detour ends; however, figure 7.7 shows that the particles continue to propagate according to the vehicle motion information after the map is re-entered. The filter manages to track the heading of the vehicle somewhat succesfully up until the northwest corner, at which case the bias in the gyroscope begins to reassert itself in the particles' trajectory as evidinced by the curve in the solution even though the vehicle truly drives in a straight line along the northern road segment.
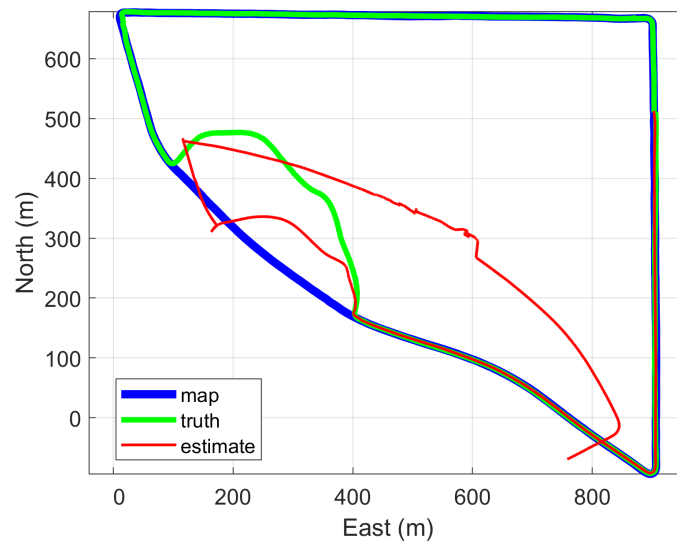

Figure 7.7: Eastside Detour with Wheel-Speed and Gyroscope-Heading: Path Visualization
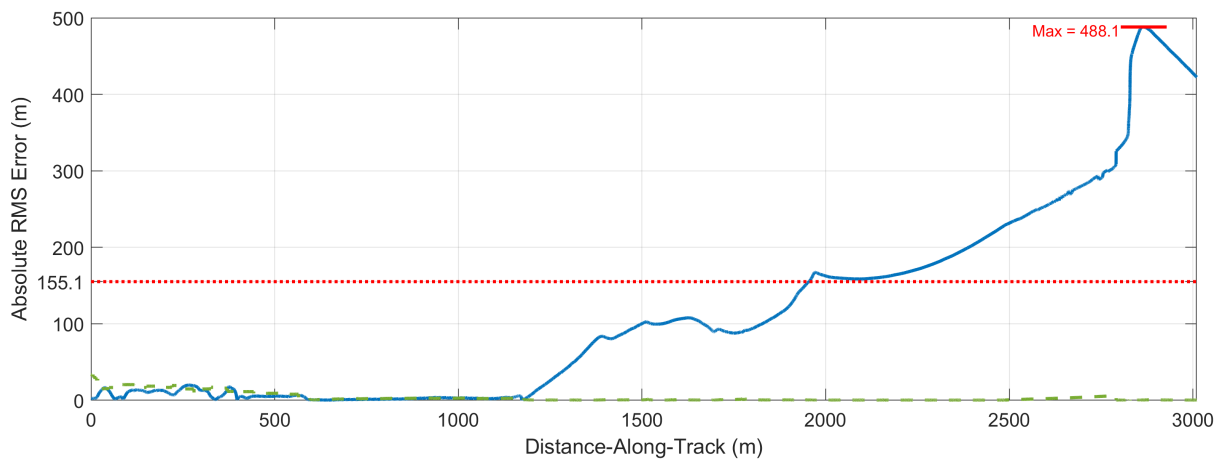

Figure 7.8: Eastside Detour with Wheel-Speed and Gyroscope-Heading: Error along track, with average error shown by the dashed red line, max error by the annotation and solid marker, and deviation of the particle spread by the dashed green line.
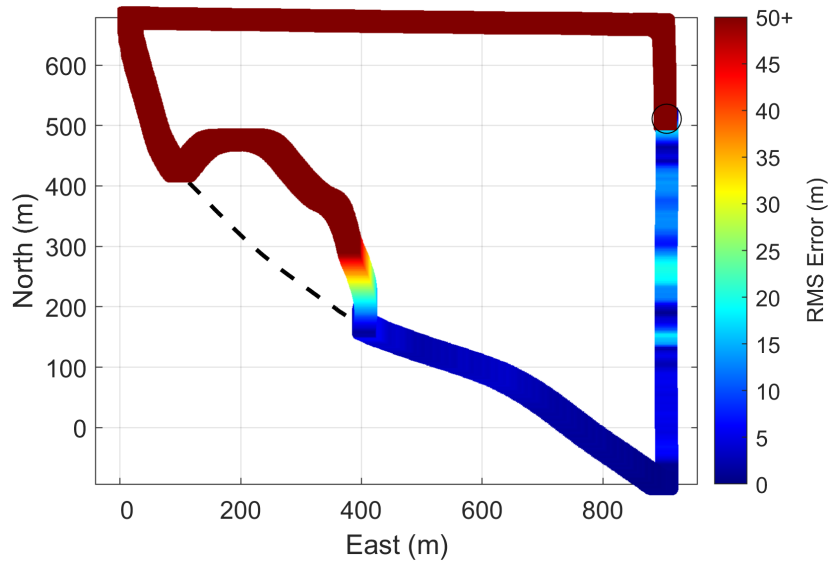
Figure 7.9: Eastside Detour with Wheel-Speed and Gyroscope-Heading: Error Color Map.

7.2 Shortcut

The second additional dataset collected was titled the 'Shortcut' set. This data set utilizes the original Eastside starting and ending positions, but turns onto a shortcut road before the second segment of the Eastside map. This shortcut road connects the first and third segments of the map, bypassing the second entirely. This shortcut is approximately 654.7 meters in length, was driven in just under 70 seconds, and featured two turns in addition to the turns necessary to enter and exit the shortcut. This segment was selected for the 'shortcut' navigation set because it bypasses a large section of the map, providing more adversity to the particle filter. Additionally, the shortcut features segments that parallel the second and first segments of the map, which could affect map-matching by exacerbating ambiguity.

7.2.1 Wheel-Speed and Mag Heading

The magnetometer-updated heading filter struggles as soon as the map is exited. The particle propagation attempts to emulate the turns and heading of the vehicle as it traverses the short-cut, but the road deweighting and map-matching likelihood steps prevent the particles from following the vehicle tooo far from the map. Unlike the detour case, in which the filter behaved erratically once the vehicle re-entered the map, the filter continues to re-create the vehicle path

Figure 7.10: Route 'Shortcut,' also beginning near the northwest corner.

after it has left the shortcut segment; however, the resulting trajectory is incorrectly scaled and at an offset from the true path driven.
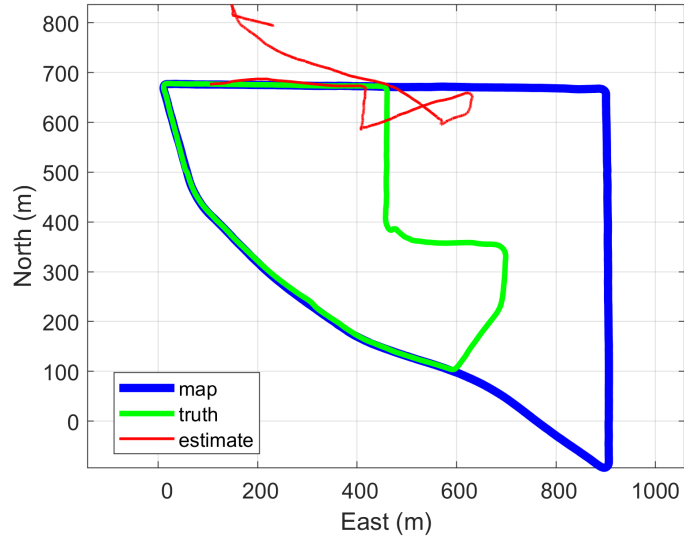
Figure 7.11: Eastside Shortcut with Wheel-Speed and Magnetometer-Heading: Path Visualization

Figure 7.12: Eastside Shortcut with Wheel-Speed and Magnetometer-Heading: Error along track, with average error shown by the dashed red line, max error by the annotation and solid marker, and deviation of the particle spread by the dashed green line.

Figure 7.13: Eastside Shortcut with Wheel-Speed and Magnetometer-Heading: Error Color Map.

7.2.2 Wheel-Speed and Gyro Heading

The gyroscope-updated heading filter also fails shortly after the shortcut begins. This version of the filter also attempts to follow the heading and geomety of the true vehicle; however, because the gyroscope cannot be reliably corrected by position updates, errors accumulate and the ultimate heading and positione estimates greatly differ from the truth.
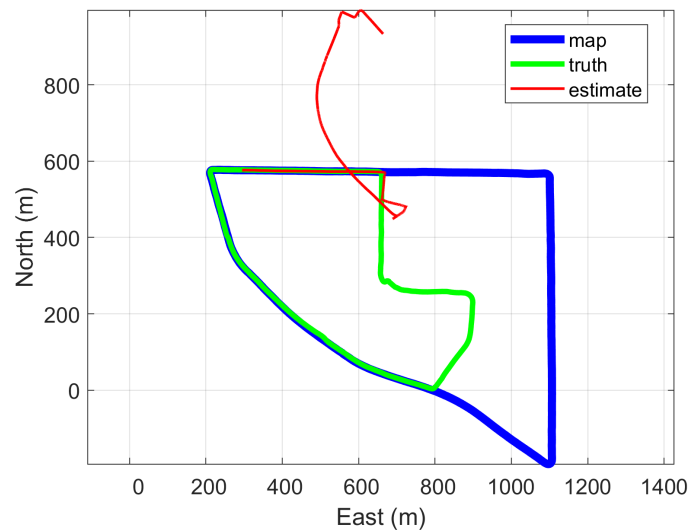
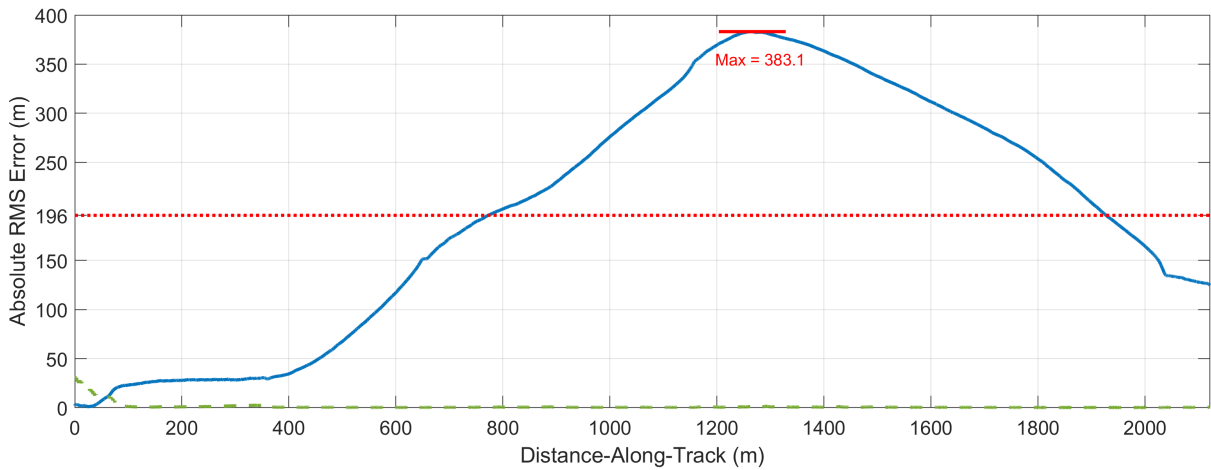Figure 7.14: Eastside Shortcut with Wheel-Speed and Gyroscope-Heading: Path Visualization

Figure 7.15: Eastside Shortcut with Wheel-Speed and Gyroscope-Heading: Error along track, with average error shown by the dashed red line, max error by the annotation and solid marker, and deviation of the particle spread by the dashed green line.
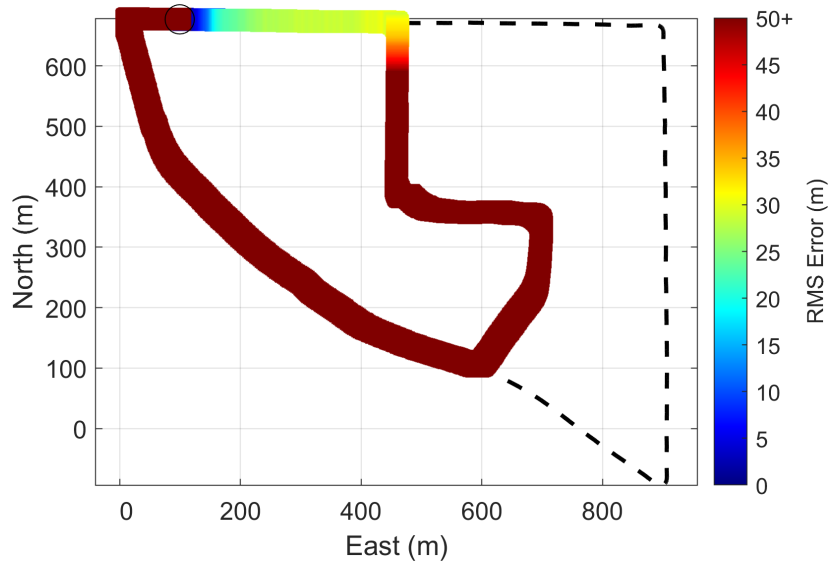

Figure 7.16: Eastside Shortcut with Wheel-Speed and Gyroscope-Heading: Error Color Map.

7.3 Reverse

The final additional dataset collected was titled the 'Reverse' set because it is the same pathway as the Eastside data set, but driven in a clockwise direction. Like before, the navigation attempt began in the northwest corner, just before the corner. It does not feature any route changes aside from directionality; however, because the data was collected on a public road, traffic lanes were adhered to so the sampled positions of the map and navigation sets do not match exactly, resulting in a minimum expected error of 1 to 3 meters.

60

7.3.1 Wheel-Speed and Mag Heading

The magnetometer-updated heading struggles immediately. Because magnetic measurements are resolved and compared *in the vehicle frame*, the direction of travel affects the likelihood evaluation step. The multivariare Gaussian likelihood function will assess two vectors that are exactly opposite in direction to be zero, virtually impossible, but the vehicle's measurements in the 'up' are minimally affected by the difference in driving direction, so the filter does not stall altogether. The function will, however, assess any position much lower due to the forward and lateral components appearing backwards with respect to the map measurements.

Despite poor matches and a turbulent trajectory estimate early in the attempt, the position estimate does eventually recovene with the vehicle as it passed the northeast corner on the final leg of the route.

Figure 7.17: Eastside Reverse with Wheel-Speed and Magnetometer-Heading: Path Visualization
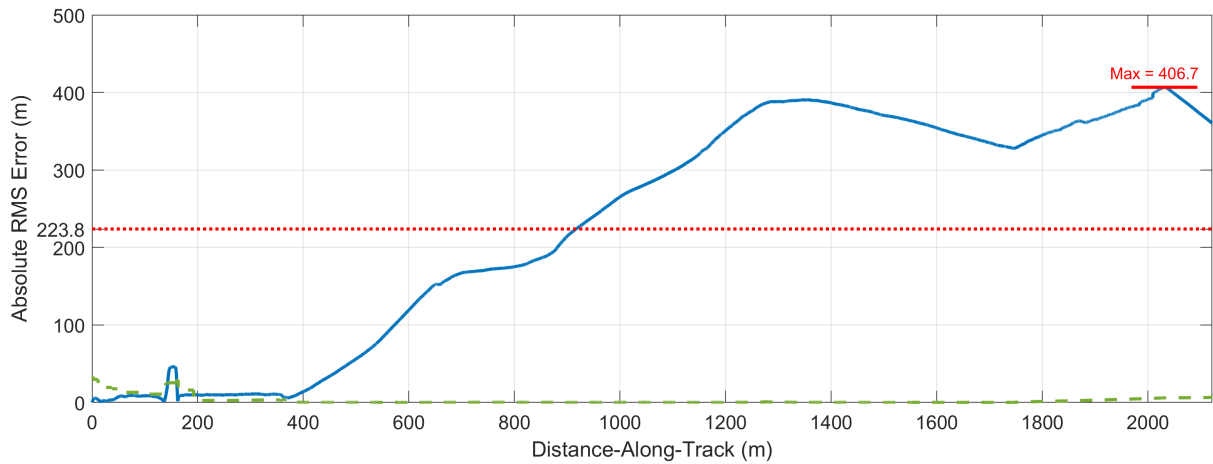
Figure 7.18: Eastside Reverse with Wheel-Speed and Magnetometer-Heading: Error along track, with average error shown by the dashed red line, max error by the annotation and solid marker, and deviation of the particle spread by the dashed green line.
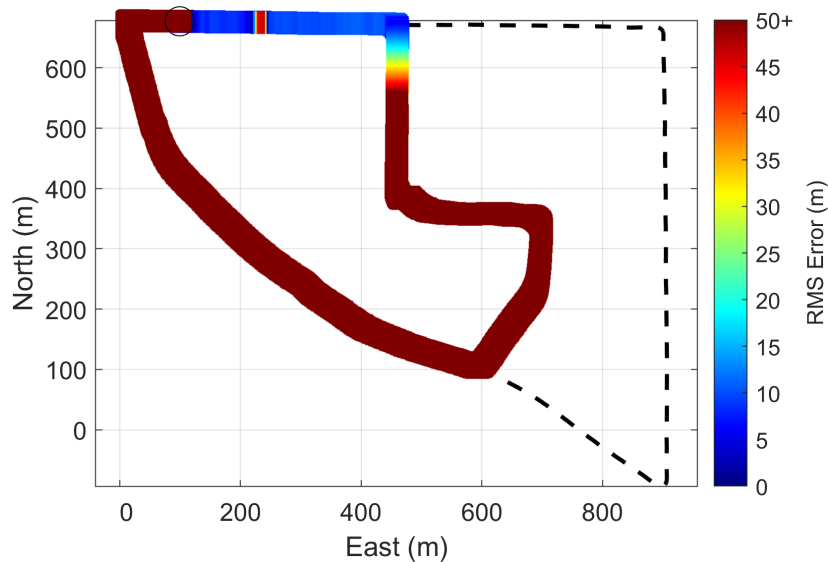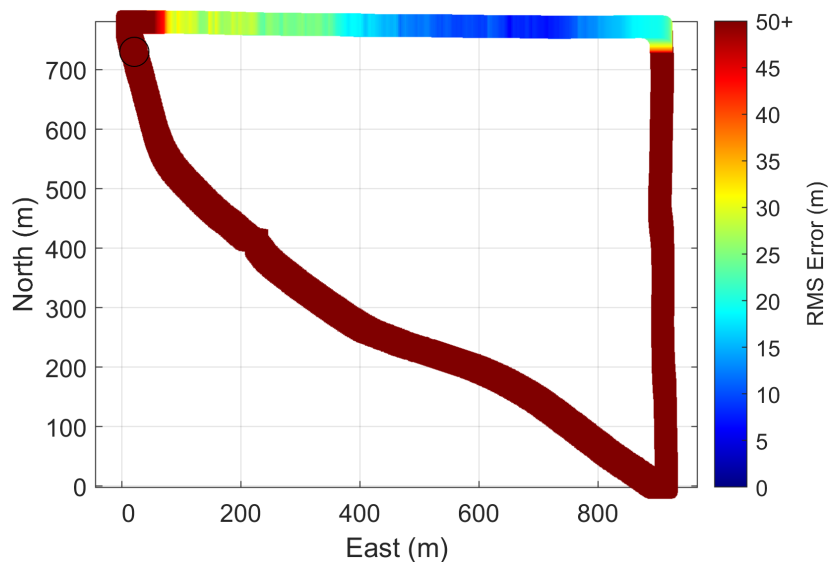

Figure 7.19: Eastside Reverse with Wheel-Speed and Magnetometer-Heading: Error Color Map.

7.3.2 Wheel-Speed and Gyro Heading

The gyroscope-updated filter, by comparison, attempted to follow the true vehicle trajectory and also did so by propagating particles off of the map, but did not succesfully recover despite eventually returning to the solutions on the map.
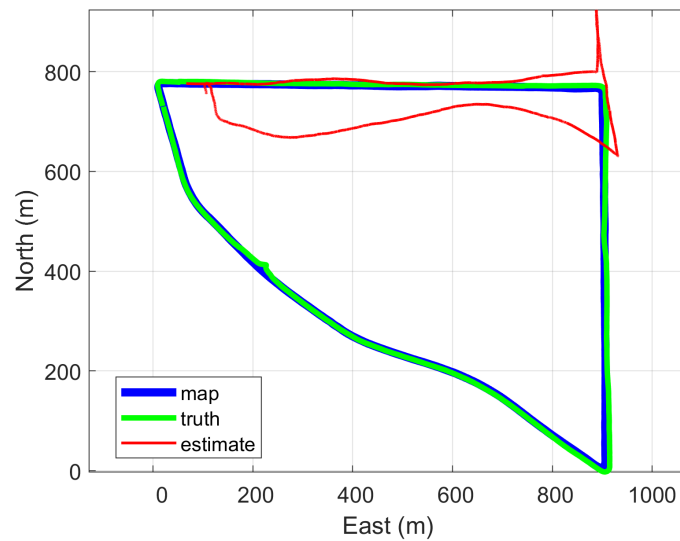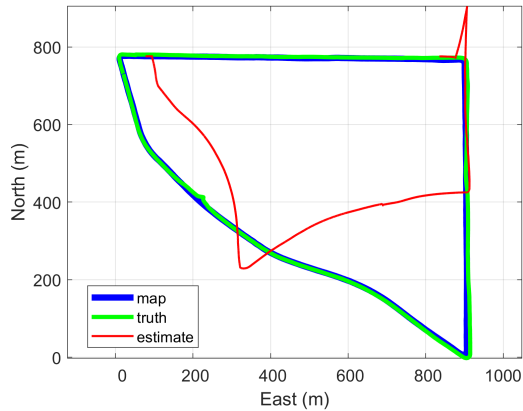
Figure 7.20: Eastside Reverse with Wheel-Speed and Gyroscope-Heading: Path Visualization.

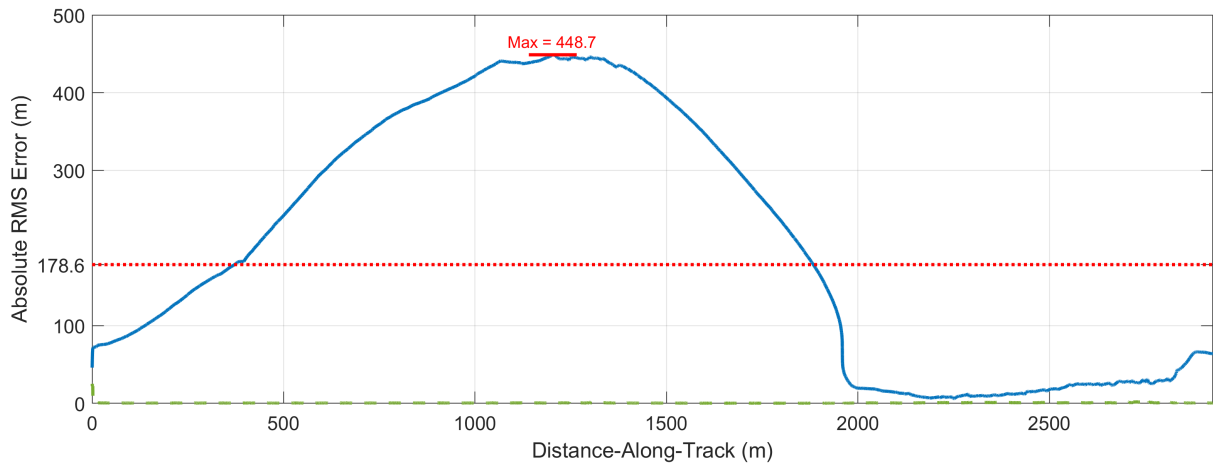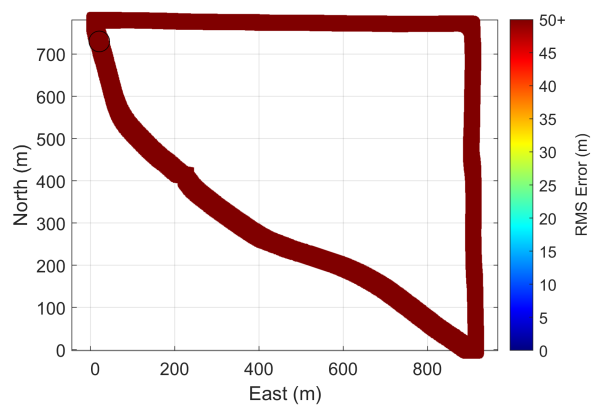Figure 7.21: Eastside Reverse with Wheel-Speed and Gyroscope-Heading: Error Color Map.
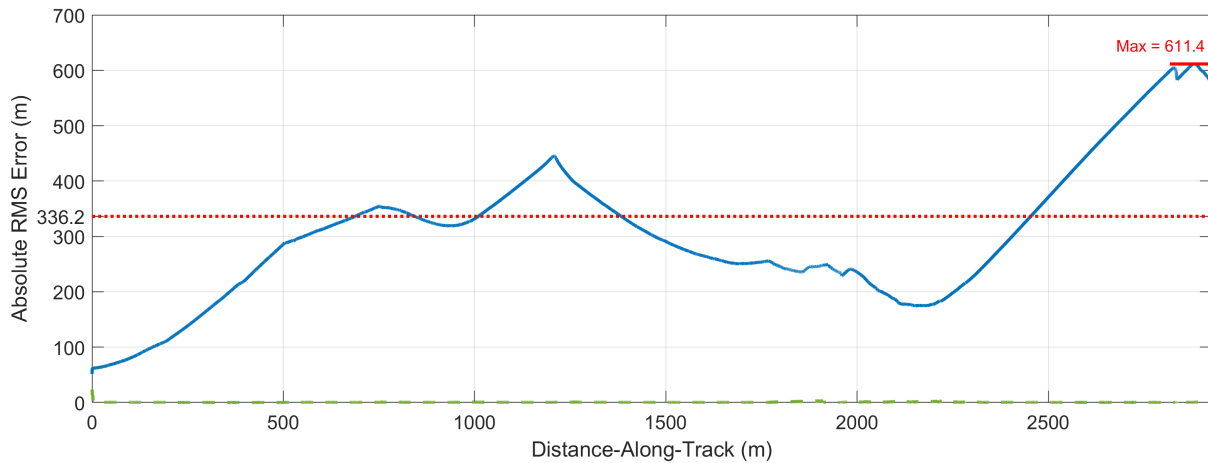
Figure 7.22: Eastside Reverse with Wheel-Speed and Gyroscope-Heading: Error along track, with average error shown by the dashed red line, max error by the annotation and solid marker, and deviation of the particle spread by the dashed green line.

7.4   Topics of Discussion

In the detour and shortcut off-route navigation attempts, each filter struggled during the off-route navigation events as expected. However, in each case, the vehicle odometry measurements provided some ability for the particles to propagate in a path that resembled the true path driven while the detour was traversed. This suggests that the particle filter may be able to rely on the vehicle motion sensors to perform mechanziation by dead-reckoning when map-matching performance is poor. However, because this would require the filter to less aggresively penalize particles that are off the map and less weight less heavily the magnetometer measurement

comparisons, these mechanization attempts were hampered by the parameter values chosen for on-route navigation.

Off-route conditions are inherently unexpected, otherwise they would be included in the map definition. Mapping every possible path or route a vehicle would be prohibitively expensive in time, storage, and configuration complexity for non-trivially sized maps; thus, designing a particle filter to perform well in off-route conditions at the expense of on-route conditions is self-defeating. Instead, an adaptive particle filter capable of modifying its own parameter values when off-route conditions are recognized may be most advantageous.

In the reverse-direction routes, the magnetometer map-matching became an even stronger detriment to the position solutions. In this case, a means of perceiving the reverse-direction might allow the filter to consider the mapped magnetic measurements alternatively by applying an additional rotation step. This could obviate the need to collect mapping data for a desired route twice, once forward and again backwards.

Chapter 8

Conclusions

Firstly, we sought to introduce new information into the particle filter using different vehicle motion models. For linear movement, a wheel-speed encoder was used to estimate the velocity of the vehicle, and for yaw, both magnetometer and gyroscope measurements were tested. These were compared to the traditional methods dead reckoning (also using either magnetometer or gyroscope for heading) and to the motion-agnostic gauss-markov particle filter developed by Shockley and Raquet. Ultimately, the wheel-speed encoder succesfully propagated particles in a way that benefited the filter by reducing the number of low-likelihood particles and of high-likelihood but low-accruacy particles. Of these, the gyroscope-derived heading update was superior to the magnetometer-derived update, but further tuning of each may bring their performances closer in line.

We also investigated the robustness of each of these methods to mapping and piloting errors by deliberately using non-matching mapping and navigation datasets. It was determined that recovery was possible for short deviations and sometimes in reverse, but not for longer deviations from the map. The magnetometer-based heading update approach was superior for off-route navigation, but the filter parameters that optimized navigation on-route did not promote optimal navigation off-route. Therefore, further research should endeavor to identify deviations from map data and apply more lenient parameter values through an adaptive filter.

A more dynamic filter would likley provide the opportunity to navigate more complex map designs, including maps that double back, intersect, or overlap. Larger and more complex maps would also require more time-consuming data collection events; however, well-implemented

filters combined with careful calibration techniques may also allow for the synthesis of disparate data sources. Since magnetometers are widely available and often already implemented on piloted and autonomous systems, maps generated could be generated from data collected by many different devices in different vehicles.

References

[1] A. Chulliat, P. Alken, and M. Nair, "The US/UK World Magnetic Model for 2020-2025: Technical Report," *Wolrd Magnetic Model*, 2020, publisher: National Centers for Environmental Information (U.S.); British Geological Survey. [Online]. Available: https://repository.library.noaa.gov/view/noaa/24390

[2] K. R. Howe, Ed., *Vaka moana: voyages of the ancestors: the discovery and settlement of the Pacific*. Honolulu: University of Hawaii Press, 2007, oCLC: ocm86109803.

[3] Meriam-Webster, "Navigation." [Online]. Available: https://www.merriam-webster.com/dictionary/navigation

[4] P. Papadimitratos and A. Jovanovic, "Protection and fundamental vulnerability of GNSS," in *2008 IEEE International Workshop on Satellite and Space Communications*. Toulouse: IEEE, Oct. 2008, pp. 167–171. [Online]. Available: http://ieeexplore.ieee.org/document/4656777/

[5] J. Zidan, E. I. Adegoke, E. Kampert, S. A. Birrell, C. R. Ford, and M. D. Higgins, "GNSS Vulnerabilities and Existing Solutions: A Review of the Literature," *IEEE Access*, pp. 1–1, 2020. [Online]. Available: https://ieeexplore.ieee.org/document/8998218/

[6] P. D. Groves, *Principles of GNSS, inertial, and multisensor integrated navigation systems*, 2nd ed., ser. GNSS technology and application series. Boston: Artech House, 2013, oCLC: ocn820530994.

[7] W. Flenniken, "Modeling Inertial Measurement Units And Analyzing The Effect Of Their Errors In Navigation Applications," Ph.D. dissertation, Auburn University, Dec. 2005. [Online]. Available: https://etd.auburn.edu/handle/10415/329

[8] A. Georgiev and P. Allen, "Localization Methods for a Mobile Robot in Urban Environments," *IEEE Transactions on Robotics*, vol. 20, no. 5, pp. 851–864, Oct. 2004. [Online]. Available: http://ieeexplore.ieee.org/document/1339385/

[9] C. Thorpe, M. Hebert, T. Kanade, and S. Shafer, "Vision and navigation for the Carnegie-Mellon Navlab," *IEEE Transactions on Pattern Analysis and Machine Intelligence*, vol. 10, no. 3, pp. 362–373, May 1988. [Online]. Available: http://ieeexplore.ieee.org/document/3900/

[10] W. H. Campbell, *Earth magnetism: a guided tour through magnetic fields*, ser. Complementary science series. San Diego: Harcourt/Academic Press, 2001.

[11] B. M. Kreutz, "Mediterranean Contributions to the Medieval Mariner's Compass," *Technology and Culture*, vol. 14, no. 3, p. 367, Jul. 1973. [Online]. Available: https://www.jstor.org/stable/3102323?origin=crossref

[12] E. Le Grand and S. Thrun, "3-Axis magnetic field mapping and fusion for indoor localization," in *2012 IEEE International Conference on Multisensor Fusion and Integration for Intelligent Systems (MFI)*. Hamburg, Germany: IEEE, Sep. 2012, pp. 358–364. [Online]. Available: http://ieeexplore.ieee.org/document/6343024/

[13] J. Haverinen and A. Kemppainen, "Global indoor self-localization based on the ambient magnetic field," *Robotics and Autonomous Systems*, vol. 57, no. 10, pp. 1028–1035, Oct. 2009. [Online]. Available: https://linkinghub.elsevier.com/retrieve/pii/S0921889009001092

[14] J. A. Shockley and J. F. Raquet, "Navigation of Ground Vehicles Using Magnetic Field Variations: Navigation of Ground Vehicles Using Magnetic Field Variations,"

Navigation, vol. 61, no. 4, pp. 237–252, Dec. 2014, this is the basis of the research. [Online]. Available: https://onlinelibrary.wiley.com/doi/10.1002/navi.70

[15] A. Canciani and J. Raquet, "Absolute Positioning Using the Earth's Magnetic Anomaly Field: Magnetic Anomaly Navigation," *Navigation*, vol. 63, no. 2, pp. 111–126, Jun. 2016. [Online]. Available: https://onlinelibrary.wiley.com/doi/10.1002/navi.138

[16] D. Broyles, K. Kauffman, J. Raquet, and P. Smagowski, "Non-GNSS Smartphone Pedestrian Navigation Using Barometric Elevation and Digital Map-Matching," *Sensors*, vol. 18, no. 7, p. 2232, Jul. 2018. [Online]. Available: http://www.mdpi.com/1424-8220/18/7/2232

[17] B. Siebler, O. Heirich, and S. Sand, "Train Localization with Particle Filter and Magnetic Field Measurements," in *2018 21st International Conference on Information Fusion (FUSION)*. Cambridge, United Kingdom: IEEE, Jul. 2018, pp. 1–5. [Online]. Available: https://ieeexplore.ieee.org/document/8455298/

[18] D. Walter, P. Groves, B. Mason, J. Harrison, J. Woodward, and P. Wright, "Road Navigation Using Multiple Dissimilar Environmental Features to Bridge GNSS Outages," in *The 28th International Technical Meeting of the Satellite Division*. Tampa, Florida: The Institute of Navigation, Sep. 2015.

[19] W. H. Campbell, *Introduction to geomagnetic fields*. Cambridge, U.K. ; New York, NY, USA: Cambridge University Press, 1997.

[20] J. H. Ginsberg, *Engineering Dynamics*. Cambridge ; New York: Cambridge University Press, 2008, oCLC: ocn123955245.

[21] G. Kitagawa, "Monte Carlo Filter and Smoother for Non-Gaussian Nonlinear State Space Models," *Journal of Computational and Graphical Statistics*, vol. 5, pp. 1–25, 1996.

[22] A. Doucet, S. Godsill, and C. Andrieu, "On sequential Monte Carlo sampling methods for Bayesian filtering," *Statistics and Computing*, vol. 10, no. 3, pp. 197–208, 2000. [Online]. Available: http://link.springer.com/10.1023/A:1008935410038

[23] "HMR2300 Smart Digital Magnetometer Datasheet," Sep. 2006. [Online]. Available: https://aerospace.honeywell.com/content/dam/aerobt/en/documents/learn/products/sensors/datasheet/SmartDigitalMagnetometerHMR2300_ds.pdf

[24] "VN-300 Dual GNSS/INS Datasheet," 2020. [Online]. Available: https://www.vectornav.com/docs/default-source/datasheets/vn-300-datasheet-rev2.pdf?sfvrsn=1e27aef3_10

[25] "TMCS1101 Hall-Effect Current Sensor," Jul. 2021. [Online]. Available: https://www.ti.com/product/TMCS1101

[26] Vectornav, "Magnetic Error Sources." [Online]. Available: https://www.vectornav.com/resources/inertial-navigation-primer/specifications--and--error-budgets/specs-magerrorsources

[27] P. S. Maybeck, *Stochastic models, estimation, and control*, ser. Mathematics in science and engineering. New York, NY: Academic press, 1982, vol. 3, no. 141-3.

[28] A. Doucet, N. Freitas, and N. Gordon, "An Introduction to Sequential Monte Carlo Methods," in *Sequential Monte Carlo Methods in Practice*, A. Doucet, N. Freitas, and N. Gordon, Eds. New York, NY: Springer New York, 2001, pp. 3–14. [Online]. Available: http://link.springer.com/10.1007/978-1-4757-3437-9_1

[29] P. Davidson, J. Collin, J. Raquet, and J. Takala, "Application of particle filters for vehicle positioning using road maps," in *Proceedings of the 23rd International Technical Meeting of The Satellite Division of the Institute of Navigation (ION GNSS+ 2010)*. Portland, Oregon: ION, Sep. 2010, pp. 1653–1661. [Online]. Available: https://www.ion.org/publications/abstract.cfm?articleID=9285

[30] M. Arulampalam, S. Maskell, N. Gordon, and T. Clapp, "A tutorial on particle filters for online nonlinear/non-Gaussian Bayesian tracking," *IEEE Transactions on Signal Processing*, vol. 50, no. 2, pp. 174–188, Feb. 2002. [Online]. Available: http://ieeexplore.ieee.org/document/978374/

[31] I. Rekleitis, "A Particle Filter Tutorial for Mobile Robot Localization TR-CIM-0402," 2003.

Appendices

Appendix A

Reverse Map Signal Augmentation

Chapter 7 demonstrated filter performance in off-route conditions and highlighted how poor trajectories were in the specific context of a route drive in the reverse direction that it was mapped. Because the magnetic field is recorded as a three-dimensional vector, directionality is embedded in the magnetic measurements associated with points on the map.

By definition, off-route contingecy conditions preclude bespoke map definitions. However, if the pilot is aware that the map will be driven in the reverse direction, the directionality of the map may be adjusted by the algorithm to account for this. This is funtinoally similar to a 180-degree rotation in the horizontal plane of each magentic measurement in the mapping data set. Figures A.1 through A.6 show the visual performance indicators for instances in which the route was driven in reverse and every horizontal magnetic measurement ('X' and 'Y' but not 'Z') of the mapping dataset was multiplied by negative one to change the sign. This approximates the signal of a mapping data set that had been driven in the opposite direction. These navigation attempts were made using the same standard-definition particle filter parameters described in chapter 6.
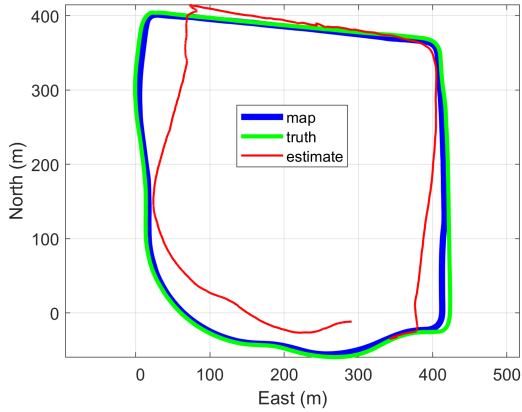
Figure A.1: VCOM Reverse, Wheel-Speed and Magnetometer-Heading with Map-Measurements Sign-Changed: Path Visualization.
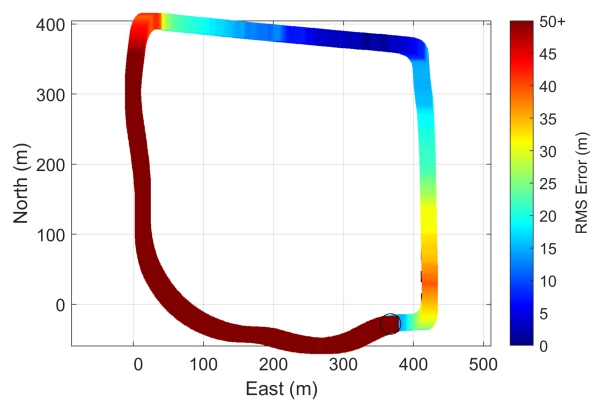

Figure A.2: VCOM Reverse, Wheel-Speed and Magnetometer-Heading with Map-Measurements Sign-Changed: Error Color Map.
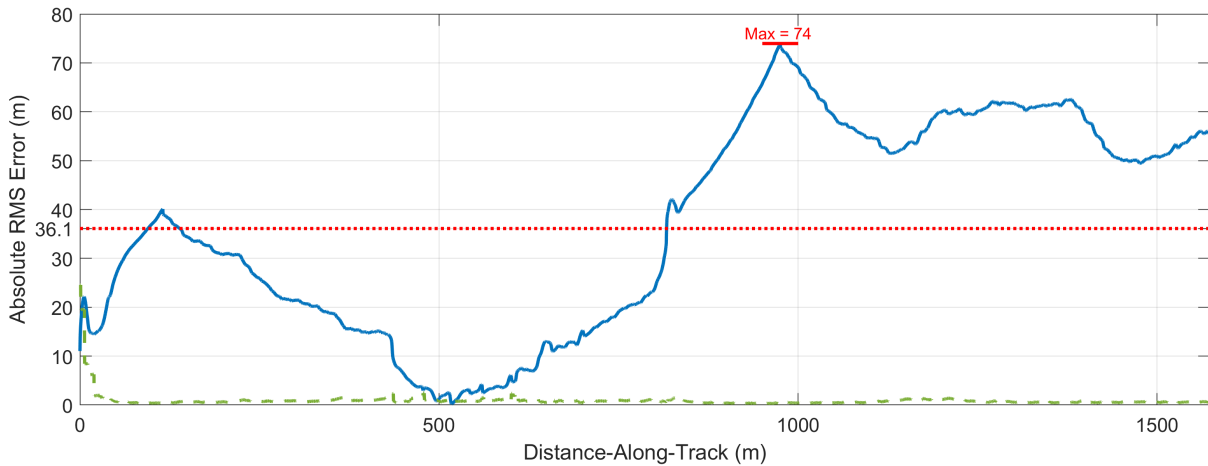

Figure A.3: VCOM Reverse, Wheel-Speed and Gyroscope-Heading with Map-Measurement Sign-Changed: Error along track

It is evident that the filter struggles early, but does recover and track the vehicle along the reverse-route after the initial turn. The magnetic heading appears to be more negatively affected by the sign-changed signal comparison, leading to the reemergence of significant error as the solution briefly stalls before the northwest corner, almost recovers again, then continues to estimate consistently off-map locations.

The gyroscope-heading-based filter is again superior to the magnetometer-heading-based filter, mostly by eliminating the off-map trajectory late in the navigation attempt. However, it does not avoid the early-run or mid-run instabilities altogether that were previously evident in the magnetometer-heading-based implementation.
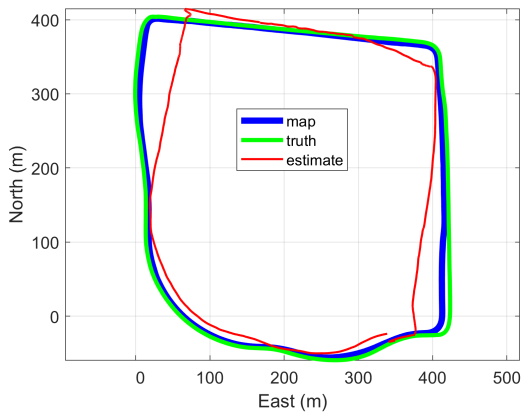
Figure A.4: VCOM Reverse, Wheel-Speed and Gyroscope-Heading with Map-Measurements Sign-Changed: Path Visualization.
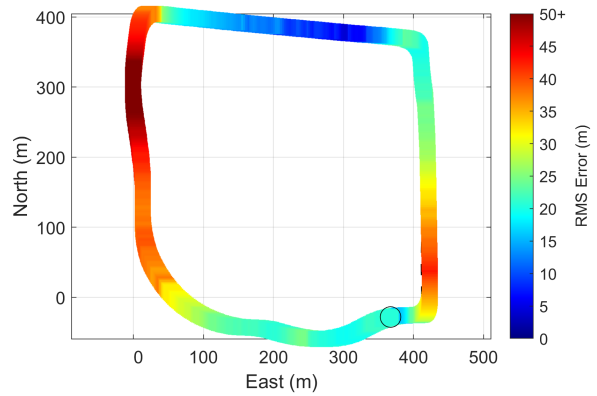

Figure A.5: VCOM Reverse, Wheel-Speed and Gyroscope-Heading with Map-Measurements Sign-Changed: Error Color Map.
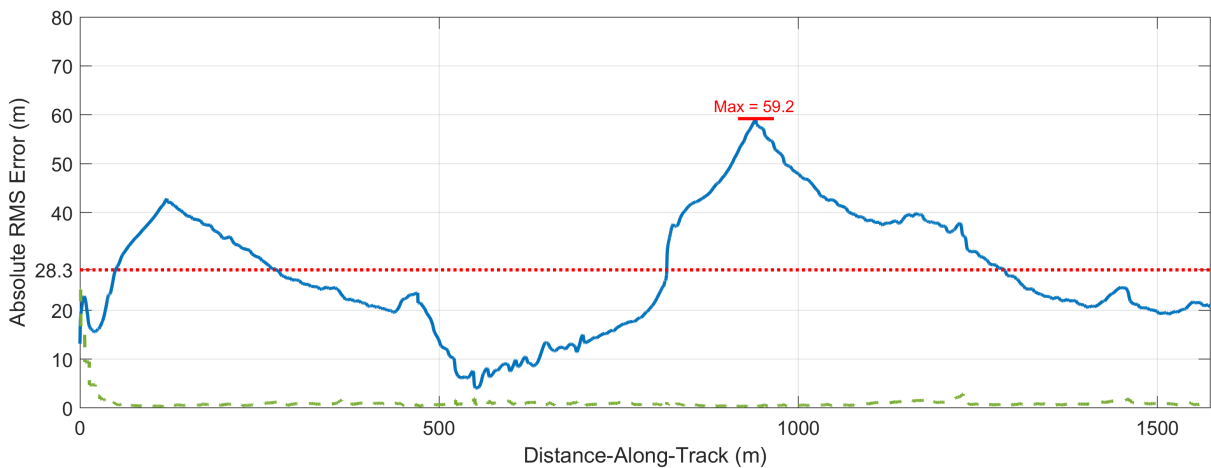

Figure A.6: VCOM Reverse, Wheel-Speed and Gyroscope-Heading with Map-Measurement Sign-Changed: Error along track

These results indicate that a magnetic map that is constructed by modifying a similar map can provide navigable solutions and is superior to an unmodified map in contingency situations. However, this approach is not a panacea and a map intentionaly constructed for the actual route driven would undoubtedly provide better overall results, but higher quality and more comprehensive maps will necessarily increase the complexity of data collection steps. This is unfeasible if maps are limited to one vehicle and sensor configuration, so a practical approach will need to source data from multiple disparate systems and sensors to provide maps and modifications of maps that are better suited to a wide range of navigation conditions.

Appendix B

Augmentation of Likelihood Techniques by Vehicle Odometry

An alternative application of vehicle motion information involves adjusting the likelihood techniques to utilize motion measurements in the process of weighting particles after they have completed the propagation step. This was investigated by comparing the accelerations of each particle at every step of the Gauss-Markov propagation method to linear acceleration information provided by the Vectornav VN-300 sensor. Because the Gauss-Markov propagation approach calculates particle accelerations in the East-North-Up tangent navigation frame, the forward and lateral acceleration of the particle must be approximated using its velocity to establish the particle's 'pseudo-vehicle frame.' Figure B.1 demonstrates how this approximate frame transformation is made.
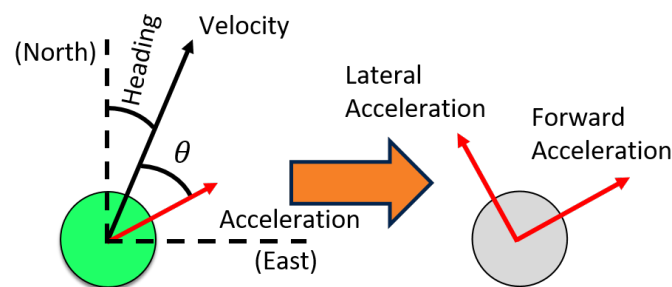

Figure B.1: Particle acceleration was assessed by approximating forward and lateral acceleration by estimating the heading from particle velocity.

The multivariate Gaussian likelihood function is again employed for the acceleration likelihood evaluation. Figure B.2 displays an example of nominal acceleration vector likelihood estimation given a virtual truth vector as the black, dashed arrow and shows the colors of the remaining arrows proportional to their likelihood as described by the colorbar. Particularly, the

arrow designated '1' is the same magnitude as the virtual truth but at a small offset angle, so it is colored solid blue to indicate fairly high likelihood. Arrow '2' is offset by a similar angle but is smaller in magnitude and so is assessed a lower likelihood. Arrow '3' is the same magnitude as virtual truth but oriented perpindicular so is considered very unlikely, but arrow '4' is shown to be slightly less unlikely, despite also being perpinduclar, due to its reduced magnitude. Arrows '5' and '6' are both very unlikely regardless of their magnitude since they are oriented opposite the virtual truth.
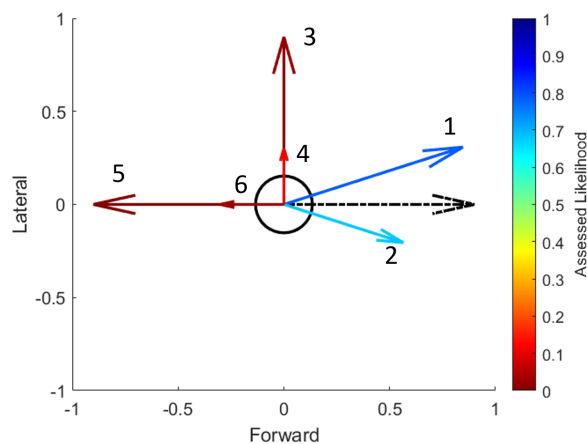

Figure B.2: An example of acceleration vectors and likelihood weightings as a function of magnitude and direction. The black, dashed-line arrow is the example truth vector.

Performance was assessed by providing the particle filter a parameter set, a map data set, a navigation data set, and a likelihood approach and associated weighting method. Each combination of interest was run 100 times and the average errors, maximum errors, and the standard deviations of the particle distributions assessed for each run.

B.1 Filter Parameters & Weighting Formulation

To achieve consistent results and improve filter stability, an additional Performance was assessed using two parameter lists corresponding to the weighting method employed:

1. Weights Update

   $n = 1000$

   Resample Percentage = 50%

   $\sigma_{road} = 6$ meters

   $\sigma_{mag} = 0.1$ Gauss

   σ_{acc} is *not* utilized

   $\sigma_{model} = 5\ m/s^2$

   $\tau = 333$ seconds

   $w_k^{(i)} = \Pi\left(L_{road}\ L_{mag}\right)$

2. Weights Overwrite

   $n = 1000$

   Resample Percentage = 0.5

   $\sigma_{road} = 6$ meters

   $\sigma_{mag} = 0.02$ Gauss

   $\sigma_{acc} = 4.0$ meters

   $\sigma_{model} = 5\ m/s^2$

   $\tau = 250$ seconds

   $w_k^{(i)} = \Pi\left(L_{road}\quad L_{mag}\ L_{acc}\right)$

It was found empirically that these parameter sets provided the best performance for their associated weighting method; however, this was not validated mathematically and further tuning for either set could improve performance.

B.2 On-Route Performance

B.2.1 Magnetometer Only, Weights Updated

The first combination of note is magnetometer-Only navigation about the VCOM route. Figure B.3 shows the status of the vehicle, particle set, and estimation overlaid above the map for three different moments in time within the best-case outcome of the 100 runs. During initialization, the particle set is distributed normally about the true starting point and are equally weighted. Partway through the filter, as the vehicle traverses the western road, the particles display some ambiguity in the estimation evidinced by the spread along the road. This ambiguity is much stronger along the eastern road; however, in neither case is it strong enough to ruin the esimation. Figure B.4 shows the component errors over the true distance traveled as well as the standard deviation of the particle set, which represents a functional uncertainty term for
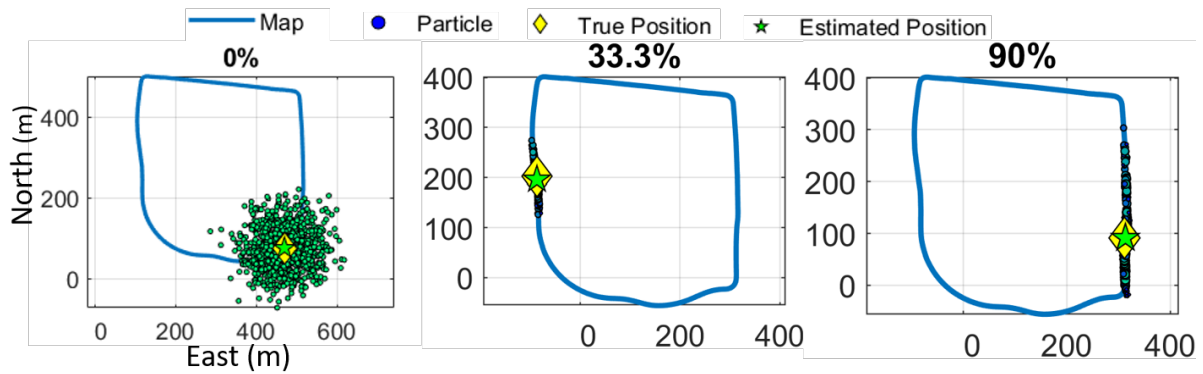
Figure B.3: Snapshots in time of the vehicle and filter status. 0% represents initialization, 33.3% and 90% refer to the approximate amount of navigation data already processed. Large, green dots are highly-weighted particles and small, blue dots are low-weighted particles.

the filter as a tightly bunched set of particles indicate a very confidents solution and a widely dispersed set indicate a solution with low confidence.
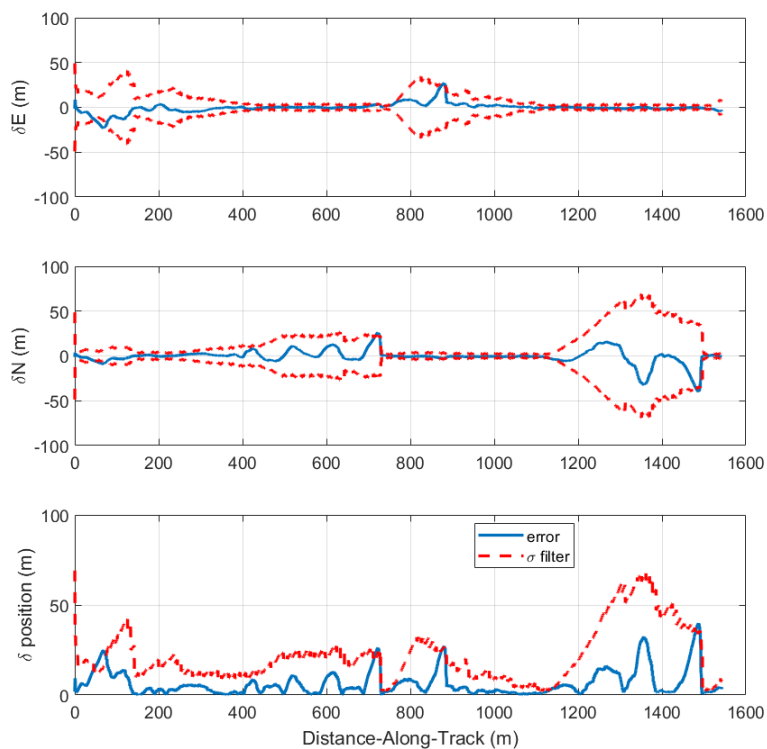

Figure B.4: VCOM map component errors compared to the true vehicle position for the **magnetometer-only**, best-case outcome. The maximum position error is 40.0 meters while the RMS error is 4.67 meters.

Table B.1 catalogs the performance statics of the filter over 100 runs of the VCOM map and navigation combination. This includes the best, average, and standard deviations of the RMS errors across all runs, and the best, average, and standard deviations of the maximum errors. This gives us insight into the typical error, approximately how reliable that error is, and the extent to which the this method struggles when it does encounter difficulty.

Table B.1: Performance indicators over 100 runs of the VCOM, **magnetometer-only** combination.

Best-Case RMS Error (m)	Average RMS Error (m)	Standard Deviation of RMS Errors (m)	Best-case Maximum Errors (m)	Average Maximum Error (m)	Standard Deviation of Max Errors (m)
4.67	6.37	1.00	34.66	57.39	17.25

B.2.2 Magnetometer and Accelerations, Weights Overwritten

Figure B.5 displays another set of snapshot of the best-case outcome of the same VCOM route, but now incorporating acceleration measurements and using the weight overwrite methodology. Initialization is functionally the same as the magnetometer-only approach. Visually, only marginal if any improvement is evident along the western road; however, the eastern road displays a significantly more confident solution and fewer particles are distributed along the road and particles are weighted more heavily nearer to the true location of the vehicle. The
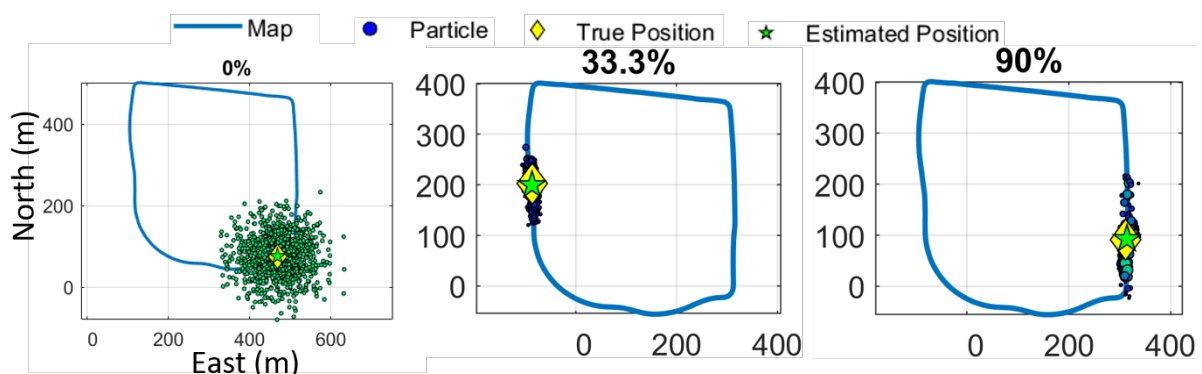

Figure B.5: Snapshots in time of the vehicle and filter status for the filter using magnetomer and acceleration data. Notice the particles are less spread out and particles more highly weighted than the magnetometer-only implementation, indicating a higher confidence.

component error trends over time, shown in Figure B.6, are not drastically different from the magnetometer-only results and the filter struggles to estimate the position of the vehcicle in approximately the same locations. However, the accelerometer-aided filter converges on a confident solution much more quickly after encountering ambiguities and reduces some of the errors encountered outside the most difficult sections.
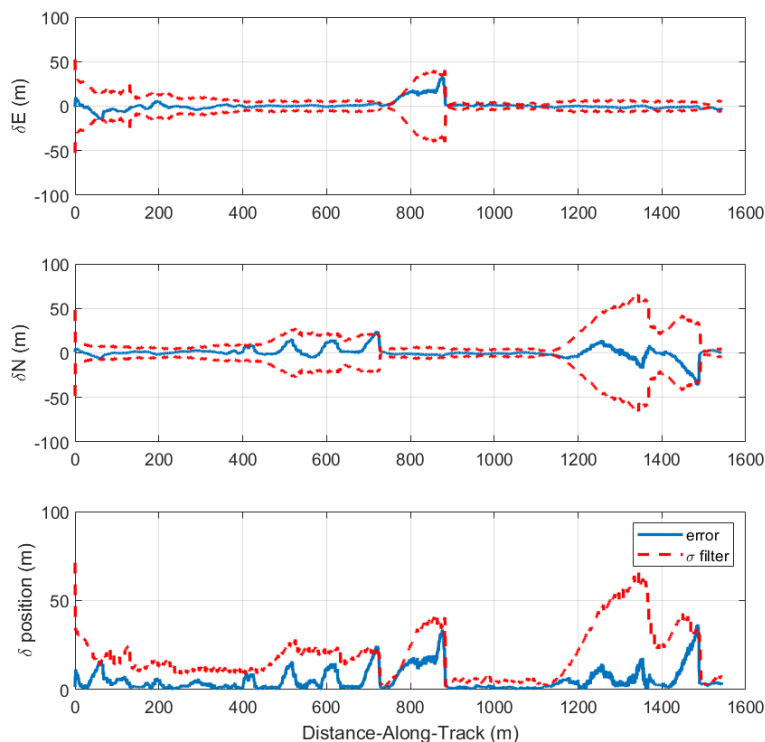

Figure B.6: VCOM map component errors for the **magnetometer-and-accelerations**, best-case outcome. The maximum position error is 36.7 meters while the error RMS is 3.85 meters.

Table B.2: Performance indicators over 100 runs of the VCOM, **magnetometer-and-accelerations** combination.

Best-Case RMS Error (m)	Average RMS Error (m)	Standard Deviation of RMS Errors (m)	Best-case Maximum Errors (m)	Average Maximum Error (m)	Standard Deviation of Max Errors (m)
3.85	5.11	0.57	35.08	52.83	20.41

Notable is the change in the best-case RMS error by -17.54%, the average RMS error by -19.80%, and the deviation of average RMS errors by -42.75%. This indicates general

improvements in the overall performance of the filter; however, the deviation of the maximum errors increases by 18.33%, indicating that the extent that the worst-case scenario strains is more variable when accelerations are utilized.

B.3 Off-Route Performance

The direct-magnetometer update approach with and without accelerometer information was again applied in the investigation of off-route performance.

B.3.1 Detour Use Case

For the detour use case, the true path driven diverged from the map provided to the filter near the end of the route. The vehicle was only briefly operated off the mapped path, approximately 60 seconds or 525 forward meters. Figures B.7 and B.8 show the true path driven with a color value at each point proportional to the error produced by the filter. The black, dashed line indicates where the map provided to the filter diverged from the true path.
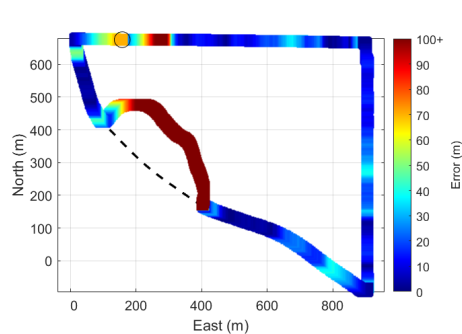

Figure B.7: Detour error-color map for the **magnetometer-only**, best-case outcome. The maximum position error is 505.11 meters while the RMS error is 47.7 meters.
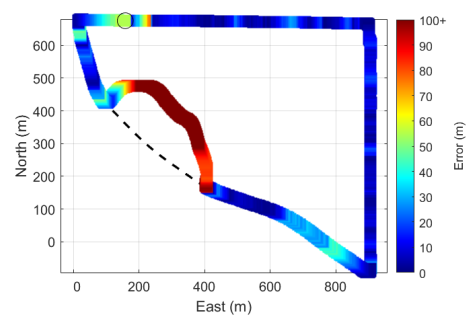
Figure B.8: Detour error-color map for the **magnetometer-and-accelerations**, best-case outcome. The maximum position error is 181.65 meters while the RMS error is 23.85 meters.

Although the accelerometer-informed filter outperforms the magnetometer-only filter in both maximum and RMS errors, some of this is due to improvements along the route before the detour is reached. Once the detour does occur, the acceleration measurements aid briefly before the filter begins to falter. Both filter types fail to provide adequate solutions while the vehicle is

off-route, but do recover once the mapped route is re-entered. The acceleration measurements do not appear to aid recovery efforts, however.

B.3.2 Shortcut Use Case

For the shortcut use case, the true path driven diverged from the map relatively early, avoiding large segments of the northern, eastner, and southern road. Figures B.9 and B.10 show the same visualization of the true-path and color-coded errors for the best-case outcome of both magnetometer-only and accelerometer-aided filters.
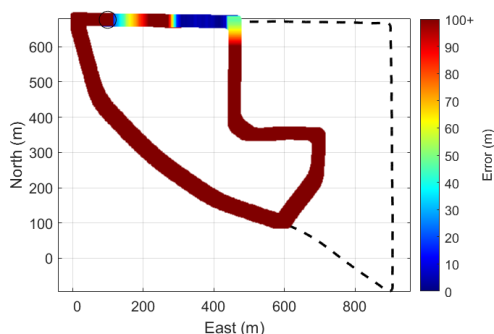

Figure B.9: Shortcut error-color map for the **magnetometer-only**, best-case outcome.
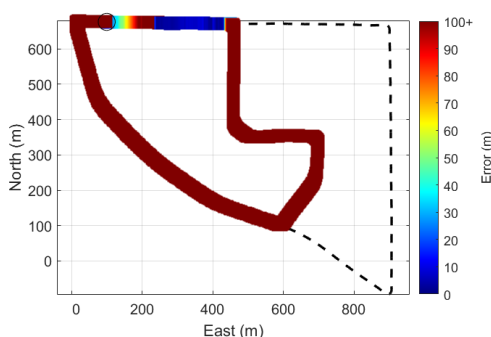
Figure B.10: Shortcut error-color map for the **magnetometer-and-accelerations**, best-case outcome.

Unlike the detour use case, the filter does not recover at any point prior to the return of the vehicle to the starting point. Additionally, the accelerations appear to slightly worsen the performance at the point of divergence with the map. Excessive resampling during the off-route navigation attempts prevented particles from propagating along the map and possibly rediscovering the vehicle once the map was re-entered.

B.4 Conclusions

This results demonstrate that the addition of accleration measurements to a magnetic map-based navigation particle filter is capable of performing at least as well as previous, unaided methods and is capable of resolving ambiguities when magnetic signals alone are insufficient.

However, this decreases the stability of the filter and can result in worse maximum errors in the worst-case scenarios.

The first-order Gauss-Markov acceleration model utilized to propagate the particles made for an especially noisy signal to compare to acceleration measurements. It may be worthwhile to implement a jerk-based propagation model to more closely shape the acceleration of the particles to motion resembling typical ground-vehicle use cases.

The lack of consideration for road grade or vehicle pitch affected the performance of the filter and would do so in many real-world use cases. This cannot be easily accounted for by tuning without affecting performance in standard, low-grade conditions. Modifying the acceleration measurements to 'flatten' the signal may improve absolute results and the reliability of the filter. This would likely require utilizing the gyroscope measurements or information from an attitude and heading reference system.

The filter as designed was only sometimes capable of recovering after encountering off-route conditions. The filter had no means of recognizing or handling this situation and instead relied on a somewhat controlled stagnation state to avoid outright divergence. This may be sufficient for brief detours, but was not at all adequate in the shortcut use case. An adaptive particle filter capable of adjusting the parameter values used to evaluate magnetometer and accelerometer measurements when off-route conditions are detected may prove more practical.